



# CHORUS

This is the accepted manuscript made available via CHORUS. The article has been published as:

## Nonreciprocal microwave transmission based on Gebhard-Ruckenstein hopping

Shumpei Masuda, Shingo Kono, Keishi Suzuki, Yuuki Tokunaga, Yasunobu Nakamura, and Kazuki Koshino

Phys. Rev. A **99**, 013816 — Published 10 January 2019

DOI: [10.1103/PhysRevA.99.013816](https://doi.org/10.1103/PhysRevA.99.013816)

# Nonreciprocal microwave transmission based on Gebhard-Ruckenstein hopping

Shumpei Masuda<sup>1,\*</sup>, Shingo Kono<sup>2</sup>, Keishi Suzuki<sup>2</sup>, Yuuki Tokunaga<sup>3</sup>, Yasunobu Nakamura<sup>2,4</sup>, and Kazuki Koshino<sup>1</sup>

<sup>1</sup>*College of Liberal Arts and Sciences, Tokyo Medical and Dental University, Ichikawa, Chiba 272-0827, Japan*

<sup>2</sup>*Research Center for Advanced Science and Technology,*

*The University of Tokyo, Meguro-ku, Tokyo 153-8904, Japan*

<sup>3</sup>*NTT Secure Platform Laboratories, NTT Corporation, Musashino 180-8585, Japan and*

<sup>4</sup>*RIKEN Center for Emergent Matter Science, Wako, Saitama 351-0198, Japan*

(Dated: December 10, 2018)

We study nonreciprocal microwave transmission based on the Gebhard-Ruckenstein hopping. We consider a superconducting device that consists of microwave resonators and a coupler. The Gebhard-Ruckenstein hopping between the resonators gives rise to a linear energy dispersion which manifests chiral propagation of microwaves in the device. This device functions as an on-chip circulator with a wide bandwidth when transmission lines are attached.

## I. INTRODUCTION

As erythrocytes transport oxygen from the lungs to the body tissues, microwaves can carry energy and information between electromagnetic components in superconducting circuits [1–6], which provide a promising platform for quantum information processing [1–3, 7–15]. Many of the quantum information processing schemes and the superconducting quantum optics experiments require routing of microwaves in a cryostat. Therefore, cryogenic circulators are indispensable tools, and the loss at each circulator is detrimental especially for quantum information processings. This motivates the growing body of experimental and theoretical works devoted to lossless on-chip microwave circulators, which possibly replace the commercial ferrite circulators.

Various principles for achieving on-chip microwave circulators, as well as their practical designs, have been proposed [16–23]. Several types of the devices with the nonreciprocal transmission of microwaves have been implemented such as, electrically driven nonreciprocity on a silicon chip [24], a circulator based on a Josephson circuit [25], a fiber-integrated quantum optical circulator operated by a single atom [26], chiral ground-state currents of interacting photons in three qubits based on a synthetic magnetic field [27], on-chip nonreciprocal current based on a combination of frequency conversion and delay [28] and the ones based on optomechanical circuits [29–31]. The nonreciprocal signal routing in photonic resonator lattice systems has been also studied [32, 33].

The Gebhard-Ruckenstein (GR) hopping [34, 35] was introduced as the hopping which gives rise to a linear energy dispersion. Model systems with the hopping was used for theoretical study of phase transitions of many-body systems. The linear energy dispersion with the fixed group velocity  $v_g = d\omega/dk$  manifests the chiral hopping of excitations in the system. Thus, the GR hopping was also used to model the helical current on the edge of a two-dimensional topological insulator [36].

In this paper, we investigate the microwave response of a system of the coupled resonators with the GR hopping. Our system functions as a circulator when transmission lines are attached to some (three or more) of the resonators. This paper is organized as follows. In Sec. II we discuss the property of the system with GR hopping. In Sec. III we introduce our circulator based on the GR hopping. In Sec. IV we analyze the microwave response of the system and demonstrate the robustness of the routing efficiency of the circulator. Section V is devoted to conclusion.

## II. GEBHARD-RUCKENSTEIN HOPPING

To illustrate the role of the GR hopping, we consider a system consisting of equally distant  $N$  sites on a ring with the GR hopping. The GR hopping gives rise to a linear energy dispersion [34, 35]. (The explicit form of the GR hopping is shown later.) A linear energy dispersion is depicted in the first Brillouin Zone (BZ) in Fig. 1(a). We consider the limit:  $N \rightarrow \infty$ , where wave number  $k$  becomes continuous, for the simplicity. There

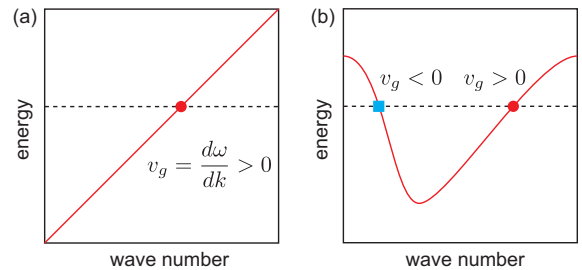


FIG. 1. Schematics of energy dispersions in the first Brillouin Zone. (a) Spectrum with linear dispersion. There is a discontinuity at the the boundary of the BZ, namely,  $E(\pi/a_L) = -E(-\pi/a_L)$ . (b) Spectrum corresponding to a system with short-range hopping. The red circle corresponds to positive group velocity, while the blue square corresponds to negative group velocity.

is a discontinuity in the spectrum at the the boundary

\* masulas@tmd.ac.jp

of the BZ,  $E(\pi/a_L) \neq E(-\pi/a_L)$ , which comes from the long-range nature of the GR hopping, where  $a_L$  is lattice parameter. There is periodicity,  $E(k+2\pi/a_L) = E(k)$ , in the extended BZ. If we take a cut of the spectrum with a fixed energy as indicated by the dashed line in Fig. 1(a), we have a single crossing point which corresponds to the group velocity,  $v_g = d\omega/dk$ , independent of  $k$ . Thus, there is no crossing point corresponding to group velocity with the opposite sign. This is the reason why there is no back scattering, and chiral current of excitation exists in this system. It is explained in Appendix A that the linear dispersion in discrete systems also gives rise to chiral current.

In contrast, the spectrum of a system with short-range hopping is a continuous function of  $k$  as depicted in Fig. 1(b). If we take a cut of the spectrum with a fixed energy we always have even number crossing points because the energy is the same at the boundary of the first BZ,  $E(\pi/a_L) = E(-\pi/a_L)$ . A half of the crossing points corresponds to positive group velocities and the rest corresponds to negative group velocities. Thus, back scattering is possible in the system.

Now we consider a system composed of  $N$  resonators with the GR hopping. A schematic of the system named GR cluster is shown in Fig. 2. The GR hopping is complex hopping, and the complex hopping can be created by periodic modulation of the coupling strength between resonators as created in various settings [27, 33, 37, 38]. Time dependent modulation of the coupling strength is the origin of the breaking of the time reversal symmetry as in the systems with a synthetic magnetic field [18, 27, 39–41].

The Hamiltonian of the GR cluster is given by

$$H_{\text{cluster}} = \sum_{m=1}^N \hbar\omega_m a_m^\dagger a_m + \sum_{m,n(\neq m)} \hbar g_{m,n}(t) a_m^\dagger a_n, \quad (1)$$

with

$$g_{m,n}(t) = 2\bar{g}_{m,n} \cos [(\omega_m - \omega_n)t + \theta_{m,n}], \quad (2)$$

where  $g_{m,n}(t)$  is periodically modulated coupling strength, and  $g_{n,m}(t) = g_{m,n}^*(t)$ . In Eq. (2),  $\bar{g}_{m,n}$  and  $\theta_{m,n}$  are time independent. Here,  $a_m$  and  $\omega_m$  are the annihilation operators of the mode of resonator  $m$  and its resonance frequency, respectively. In the rotating frame, the effective Hamiltonian is represented as

$$H_{\text{cluster}} = \sum_{m,n(\neq m)} \hbar(\bar{g}_{m,n} e^{-i\theta_{m,n}}) a_m^\dagger a_n. \quad (3)$$

The GR hopping is defined by

$$\bar{g}_{m,n} e^{-i\theta_{m,n}} = \tilde{g}_{m,n} = \begin{cases} \frac{i\pi\eta_0(-1)^{n-m}}{N \sin \frac{\pi(n-m)}{N}} & (n \neq m) \\ 0 & (n = m) \end{cases}, \quad (4)$$

where  $\eta_0$  is a real constant.

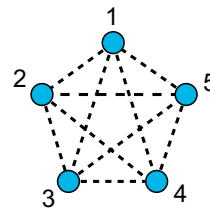


FIG. 2. Schematic of a GR cluster for  $N = 5$ . The blue circles represent resonators. The dashed lines represent the coupling between the resonators.

The single-particle eigenstates and their eigenenergies are represented as

$$|\nu\rangle = \sum_{m=1}^N \phi_\nu(m) |m\rangle, \\ E_\nu = \hbar\eta_0 k_\nu, \quad (5)$$

respectively, with the wave function  $\phi_\nu(m) = \frac{1}{\sqrt{N}} \exp(ik_\nu m)$ , where  $\nu = -(N-1)/2, \dots, (N-1)/2$  for odd  $N$ , and  $\nu = -N/2, \dots, N/2 - 1$  for even  $N$ . Here,  $|m\rangle$  represents the state in which the particle (photon) is localized at resonator  $m$ .  $k_\nu$  is given by  $k_\nu = 2\pi\nu/N$  for odd  $N$ , and  $k_\nu = 2\pi(\nu + 1/2)/N$  for even  $N$ .

Figures 3(a) and 3(b) show  $\tilde{g}_{m,n}/(i\eta_0)$  for  $N = 9$  and 8, respectively. The sign of  $\tilde{g}_{m,n}$  changes alternately with respect to the resonator number  $n$  (except for  $n = N$  for even  $N$ ). Note that the coupling constants are cyclic for odd  $N$ , that is,  $\tilde{g}_{m,n} = \tilde{g}_{m+j,n+j}$  for integer  $j$ , where the indices are understood modulo  $N$ . In contrast, this does not hold for even  $N$ :  $\tilde{g}_{N,1} = -\tilde{g}_{1,2}$  (see Fig. 3(b)).

Figures 4(a) and 4(b) plot the eigenenergies as the functions of wave number. Figures 4(c) and 4(d) show the phase of the wave function of the fourth lowest level relative to that of site 1. The phase of the wave function of the eigenstates changes approximately  $2\pi\nu$  from site 1 to site  $N$  for odd  $N$ , while it changes approximately  $2\pi(\nu + 1/2)$  for even  $N$  as shown in Figs. 4(c) and 4(d).

In Fig. 5, we observe the dynamics of a particle (photon) in the GR clusters. The initial state is set as  $|\Psi\rangle = |1\rangle$ . Figures 5(a) and 5(b) show the time-evolution of the population at each resonator for the systems with  $N = 5$  and 6, respectively. The figures clearly show the chiral population transfer in the GR clusters.

### III. CIRCULATOR BASED ON GR HOPPING

In this section, we propose a way of routing microwaves based on the GR hopping between resonators. As depicted in Fig. 6, our system consists of the  $N$  resonators with different resonance frequencies, a coupler of the resonators and transmission lines coupled to some of the resonators. We assume that each resonator is coupled to the other resonators with time-dependent coupling strength,

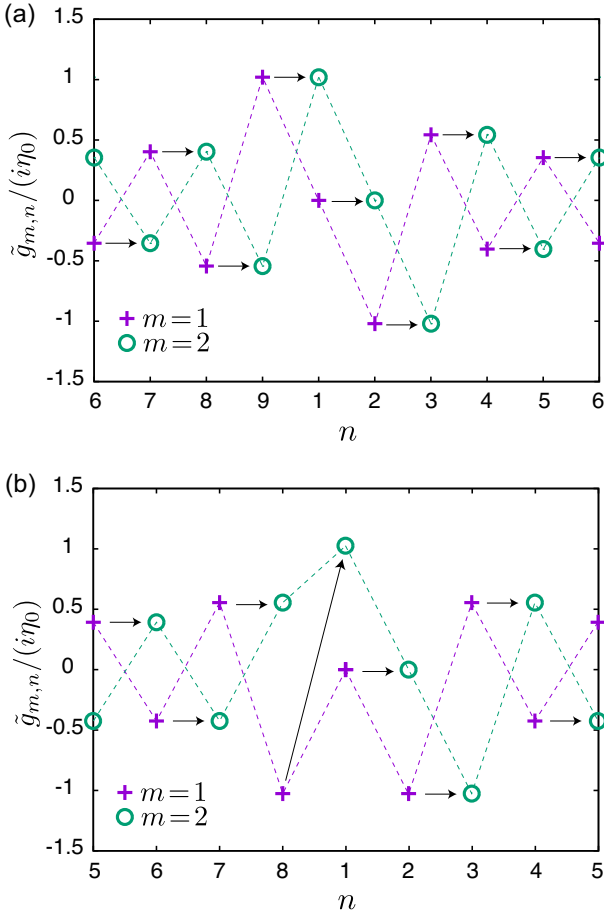


FIG. 3. Coupling constant in the GR model.  $\tilde{g}_{m,n}$  for  $m = 1, 2$  are shown for  $N = 9$  and  $8$  in panels (a) and (b), respectively. Note that the rightmost and leftmost values in the panels are identical. The dashed lines are the guide to the eyes. The arrows in panel (a) indicate the cyclicity of the Hamiltonian elements for  $N = 9$ , and the arrows in panel (b) indicate the lack of the cyclicity for  $N = 8$ .

and they form a GR cluster. (Physical realization is discussed in Appendix G.) The Hamiltonian of the system is given by

$$\begin{aligned}
 \mathcal{H} &= \mathcal{H}_{\text{cluster}} + \mathcal{H}_{\text{damp}}, \\
 \mathcal{H}_{\text{cluster}} &= \sum_{m=1}^N \hbar\omega_m a_m^\dagger a_m + \sum_{m,n(\neq m)}^N \hbar g_{m,n}(t) a_m^\dagger a_n, \\
 \mathcal{H}_{\text{damp}} &= \hbar \sum_{m=1}^N \int dk \left[ v k b_{m,k}^\dagger b_{m,k} \right. \\
 &\quad \left. + \sqrt{\frac{v\kappa_m}{2\pi}} (a_m^\dagger b_{m,k} + b_{m,k}^\dagger a_m) \right]. \quad (6)
 \end{aligned}$$

Here,  $\mathcal{H}_{\text{cluster}}$  is the Hamiltonian of the GR cluster defined in Eq. (1) with the periodically modulated coupling given by Eqs. (2) and (4), and  $\mathcal{H}_{\text{damp}}$  describes the interactions between the transmission lines and the resonator

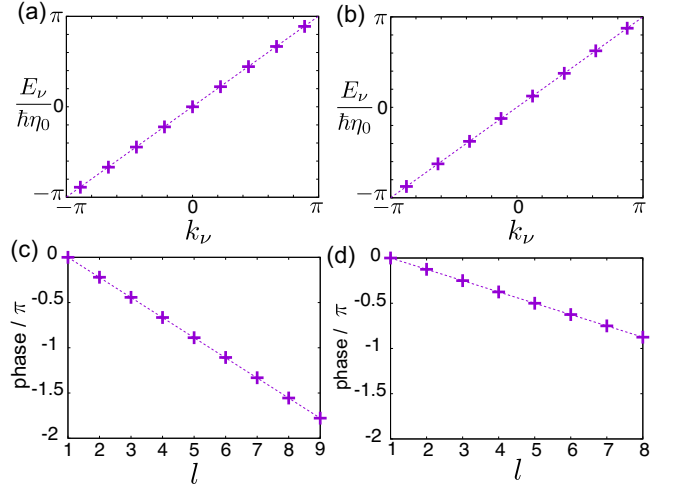


FIG. 4. Eigenenergies of  $H_{\text{cluster}}$  as the functions of  $k_\nu$  for (a)  $N = 9$  and (b)  $N = 8$ . Panels (c) and (d) show the phase of wave function  $\phi_{-1}(l)$  relative to that of  $\phi_{-1}(1)$  for  $N = 9$  and  $8$ , respectively. The dashed lines are the guide to the eyes.

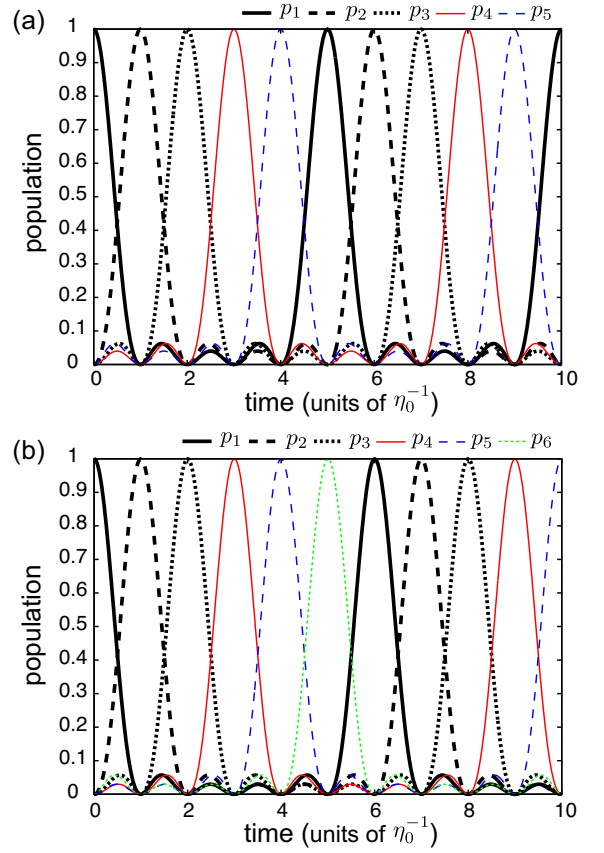


FIG. 5. Time-evolution of the population at each site for the systems with (a)  $N = 5$  and (b)  $N = 6$ .  $p_i$  denotes the population of resonator  $i$ .

modes.  $b_{m,k}$  is the mode of the transmission line  $m$  with

wave number  $k$ . We refer to the transmission line attached to resonator  $m$  as transmission line  $m$ .  $v$  is the microwave velocity in the transmission lines, and  $\kappa_m$  is the decay rate of a photon from resonator  $m$  into transmission line  $m$ . Note that transmission lines are not attached to some of the resonators. For example, in Fig. 6,  $\kappa_2 = \kappa_5 = 0$ .

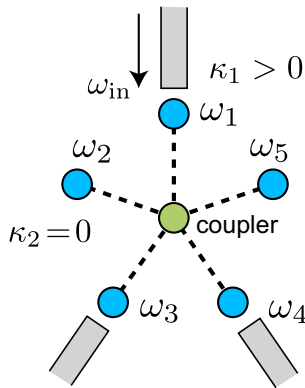


FIG. 6. Schematic of a circulator with  $N = 5$ . The input field is applied through one of the transmission lines. The blue circles, the green circle and gray lines represent the resonators, the coupler, and the transmission lines, respectively. The dashed lines represent the coupling between the resonators. Transmission lines are uncoupled to resonators 2 and 5 in this example.

We comment here on the relation between our circulator and that studied previously. The  $N = 3$  case was studied in Ref. 27 to show that the circulating a microwave photon is achieved with complex hopping. Our circulator based on the GR hopping for  $N = 3$  with  $\eta_0 = 3g \sin(\pi/3)/\pi$  and  $\kappa_m = 2g$  reduces to the same system, where  $g$  is constant.

#### IV. RESULTS

Wide bandwidth is a desirable property of a circulator. We examine the stability of the routing efficiency against detuning of the incident microwaves. The amplitude of the coupling between resonators  $|\tilde{g}_{m,n}|$  in Eq. (4) depends on  $m$  and  $n$ . It is seen from Eq. (4) that the nearest neighbor coupling of the GR cluster is the largest. Hereafter, the amplitude of the nearest neighbor hopping is fixed to be  $g$  irrespectively of  $N$ , that is,  $|\tilde{g}_{m,m+1}| = |\tilde{g}_{m+1,m}| = g$ , where the subscripts are modulo  $N$ , and  $g$  is used as the unit of detuning. We consider the case in which every transmission line is coupled to a resonator with the same strength,  $\kappa$ , unless it is stated that we consider other cases. In the following, we first present the results for odd  $N$ , and then show the results for even  $N$ .

#### A. S-matrix

We consider the injection of continuous microwave from one of the transmission lines, transmission line  $p$ . As shown in Appendix B, the transmission and reflection coefficients of the microwave are given by the  $S$ -matrix elements represented as

$$S_{p,m} = \delta_{p,m} - \sqrt{\kappa_p \kappa_m} [\mathcal{G}^{-1}]_{m,p}, \quad (7)$$

where  $[\mathcal{G}^{-1}]_{m,p}$  is the element of matrix  $\mathcal{G}^{-1}$ . The elements of matrix  $\mathcal{G}$  are given by

$$\mathcal{G}_{m,n} = \begin{cases} \kappa_m/2 - i\Delta\omega & (n = m), \\ i\tilde{g}_{m,n} e^{-i\theta_{m,n}} & (n \neq m), \end{cases} \quad (8)$$

where  $\Delta\omega (\equiv \omega_{\text{in}} - \omega_p)$  is the detuning of the incident microwave, and  $\omega_{\text{in}}$  is the frequency of the incident microwave.

#### B. three-resonator system

For the reference, we examine the routing efficiency of the three-resonator system. Figure 7(a) shows the dependence of the forward transmission probabilities (counter clockwise) on  $\kappa$  for  $N = 3$  without detuning. The forward transmission probabilities become unity at  $\kappa = 2g$ . Figure 7(b) shows the dependence of the forward and backward transmission and reflection probabilities on detuning  $\Delta\omega$  with  $\kappa = 2g$ .

#### C. five-resonator system

Figure 8(a) shows the dependence of the forward transmission probabilities on  $\kappa$  for  $N = 5$  without detuning,  $\Delta\omega = 0$ . The transmission lines are coupled to resonators 1, 3 and 4. We numerically confirm that  $|S_{13}| = |S_{34}| = |S_{41}|$ . These equalities are analytically derived in Appendix D. The forward transmission probabilities become unity at  $\kappa = 4g$ . This value of  $\kappa$  is twice larger than the ideal value of  $\kappa (= 2g)$  for  $N = 3$ . Figure 8(b) shows the dependence of the forward and backward transmission and reflection probabilities on detuning  $\Delta\omega$  with  $\kappa = 4g$ . It is seen that the forward transmission probabilities for  $N = 5$  are higher than that for  $N = 3$ .  $S_{33}$  and  $S_{44}$  ( $S_{43}$ ) exhibit similar  $\Delta\omega$ -dependence to  $S_{11}$  ( $S_{14}$  and  $S_{31}$ ), and they are not shown here.

The robustness of the routing efficiency against detuning depends on which resonators the transmission lines are attached to. In Fig. 9, we make the same plot as Fig. 8 except that the transmission lines are attached to resonators 1,2 and 5. Figure 9(a) shows the dependence of the forward transmission probabilities on  $\kappa$ . The optimal value of  $\kappa$ , with which  $|S_{12}|$ ,  $|S_{25}|$ , and  $|S_{51}|$  become unity, is approximately  $2.472g$ . Figure 9(b) shows the dependence of the forward and backward transmission and

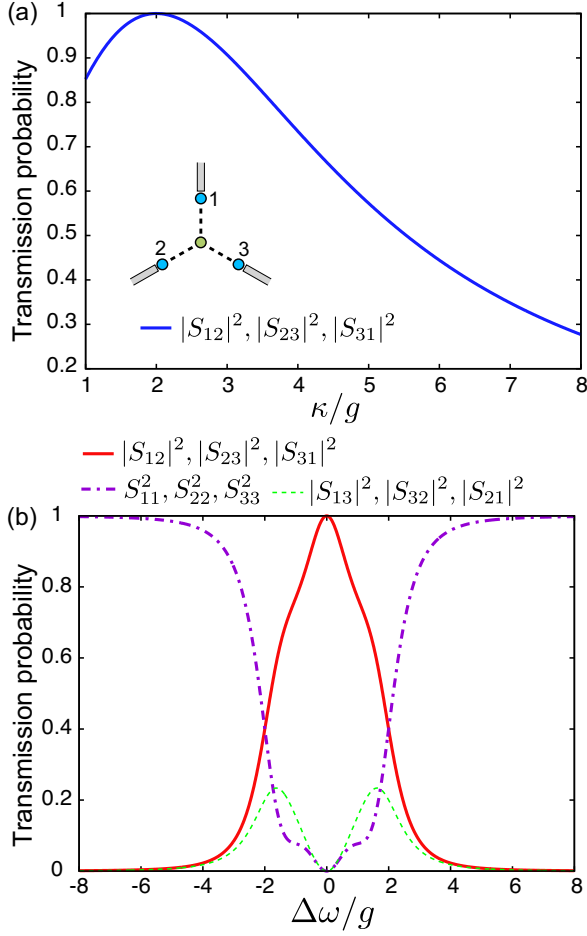


FIG. 7. Circulation properties for the case of  $N = 3$  and  $\kappa_{1,2,3} = \kappa$ . (a) Dependence of the forward transmission probabilities ( $|S_{12}|^2$ ,  $|S_{23}|^2$  and  $|S_{31}|^2$ ) on  $\kappa$  for  $\Delta\omega = 0$ . The inset shows the system configuration. (b) Dependence of the forward and backward transmission and reflection probabilities on  $\Delta\omega$  for  $\kappa = 2g$ .

the reflection probabilities on detuning for  $\kappa = 2.472g$ . The transmission probabilities are comparable to that for  $N = 3$  for  $|\Delta\omega/g| < 0.5$  as seen in the inset of Fig. 9(b). Therefore, the configuration in Fig. 8(a) is more desirable than the one in Fig. 9(a).  $S_{22}$  and  $S_{55}$  ( $|S_{52}|$ ) exhibit a similar  $\Delta\omega$ -dependence to  $S_{11}$  ( $|S_{15}|$  and  $|S_{21}|$ ), and they are not shown here. The results for  $N = 7$  system is shown in Appendix C.

#### D. four-resonator system

Figure 10(a) shows the dependence of the forward transmission probabilities on  $\kappa$  for  $N = 4$  without detuning. The transmission lines are coupled to resonators 1, 2 and 4. Under the condition of  $\kappa_1 = \kappa_2 = \kappa_4$ , it is seen that  $S_{12}$ ,  $S_{24}$ ,  $S_{41}$  do not reach unity simultaneously. Therefore, this system does not work as a circulator.

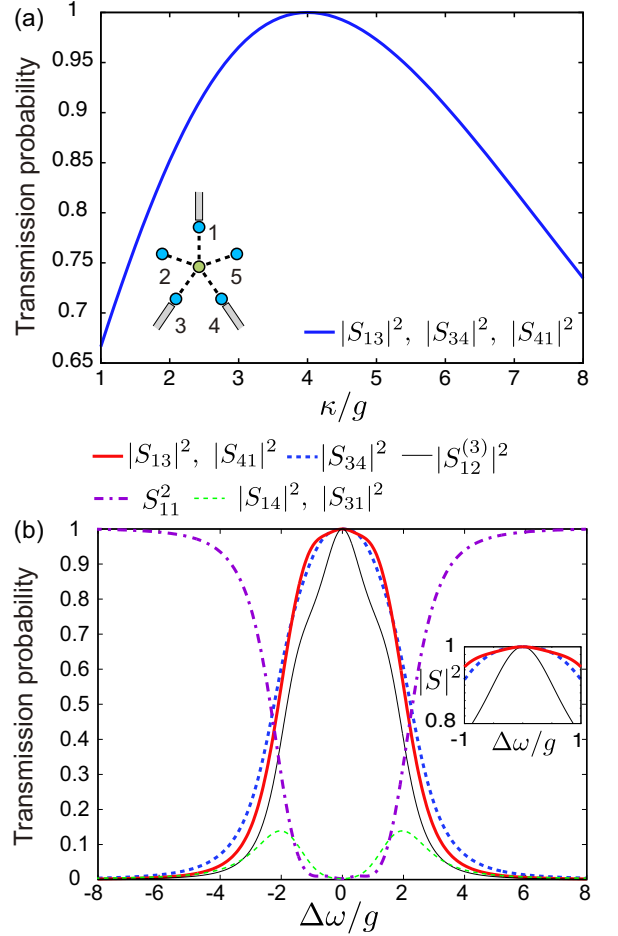


FIG. 8. Circulation properties for the case of  $N = 5$ ,  $\kappa_{1,3,4} = \kappa$ , and  $\kappa_{2,5} = 0$ . (a) Dependence of the forward transmission probabilities ( $|S_{13}|^2$ ,  $|S_{34}|^2$  and  $|S_{41}|^2$ ) on  $\kappa$  for  $\Delta\omega = 0$ . The inset shows the system configuration. (b) Dependence of the forward and backward transmission and reflection probabilities on  $\Delta\omega$  for  $\kappa = 4g$ . The thin black line represents  $|S_{12}|^2$  for  $N = 3$ , denoted by  $|S_{12}^{(3)}|^2$ . The inset is a closeup around  $\Delta\omega/g = 0$ .

Now we consider the case with  $\kappa_1 \neq \kappa_2 = \kappa_4$ . We optimize  $\kappa_1$  and  $\kappa_2$  so that the product of the forward transmission amplitudes defined by  $|S_{12}S_{24}S_{41}|$  is maximized. Figure 10(b) shows the dependence of the forward and backward transmission and reflection probabilities on the detuning for  $\kappa_1 = 2.14g$  and  $\kappa_{2,4} = 4.24g$ . It is seen that the forward transmission probabilities are almost unity for  $\Delta\omega = 0$ , and the routing efficiency is robust against the detuning more than the circulator for  $N = 3$ .  $S_{22}$  and  $S_{44}$  ( $|S_{42}|$ ) show a similar  $\Delta\omega$ -dependence to  $S_{11}$  ( $|S_{14}|$  and  $|S_{21}|$ ), and they are not shown here.

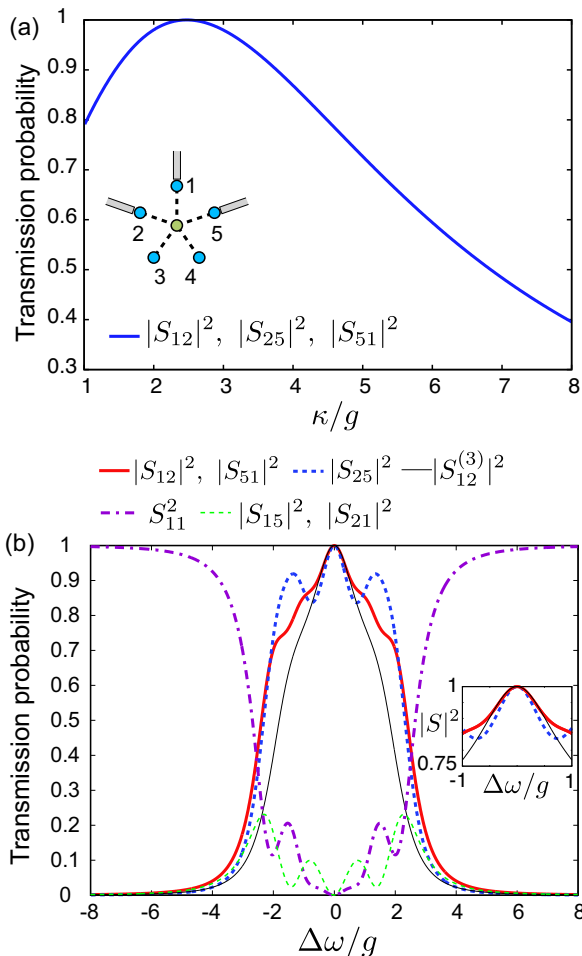


FIG. 9. Circulation properties for the case of  $N = 5$ ,  $\kappa_{1,2,5} = \kappa$ , and  $\kappa_{3,4} = 0$ . (a) Dependence of the forward transmission probabilities ( $|S_{12}|^2$ ,  $|S_{25}|^2$  and  $|S_{51}|^2$ ) on  $\kappa$  for  $\Delta\omega = 0$ . The inset shows the system configuration. (b) Dependence of the forward and backward transmission and reflection probabilities on  $\Delta\omega$  for  $\kappa = 2.472g$ . The black line represents  $|S_{12}^{(3)}|^2$ . The inset is a closeup around  $\Delta\omega/g = 0$ .

### E. six-resonator system

Figure 11(a) shows the dependence of the transmission probabilities on  $\kappa$  for  $N = 6$  without detuning. The transmission lines are coupled to resonators 1, 3 and 5. As expected from the rotational symmetry,  $|S_{13}| = |S_{35}| = |S_{51}|$ . The transmission probabilities become unity when  $\kappa \simeq 4.328g$ .

Figure 11(b) shows the dependence of the transmission and reflection probabilities on the detuning for  $\kappa = 4.328g$ . As seen in the inset, the routing efficiency is obviously robust against the detuning compared to the systems with other cavity number  $N$ . The effects of fluctuations of the system parameters is examined in Appendix F.

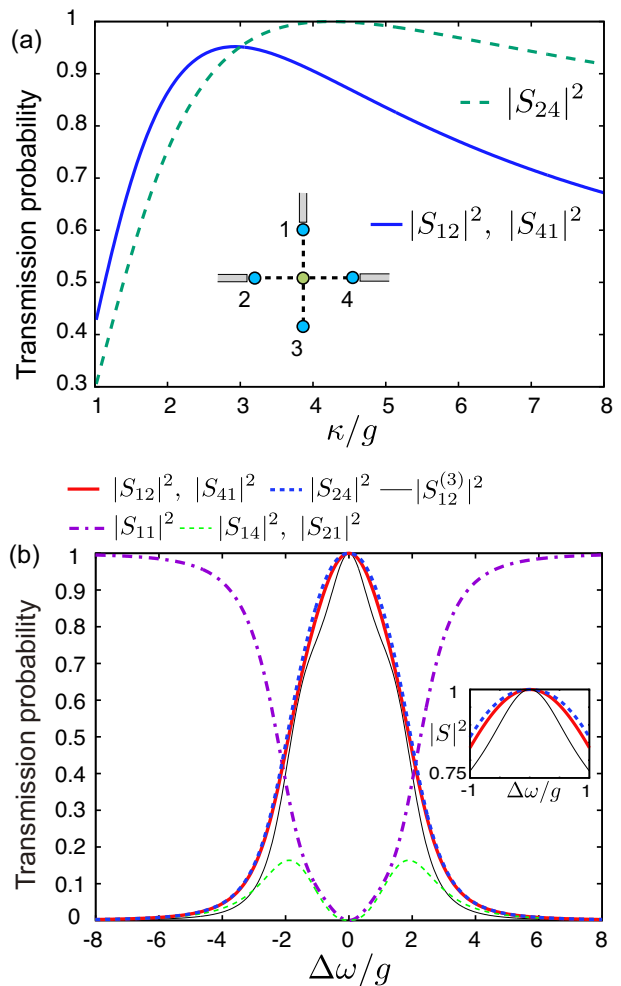


FIG. 10. Circulation properties for the case of  $N = 4$  and  $\kappa_3 = 0$ . (a) Dependence of the forward transmission probabilities ( $|S_{12}|^2$ ,  $|S_{41}|^2$  and  $|S_{24}|^2$ ) on  $\kappa$  for  $\Delta\omega = 0$  when  $\kappa_{1,2,4} = \kappa$ . The inset shows the system configuration. (b) Dependence of the forward and backward transmission and reflection probabilities on  $\Delta\omega$  for the case of  $\kappa_1 = 2.14g$  and  $\kappa_{2,4} = 4.24g$ .

### F. Systems with large number of resonators

To see an asymptotic property we examine large  $N$  systems. The transmission lines are attached in a way that the system is geometrically symmetric against  $2\pi/3$  rotation for concreteness. Figure 12(a) shows the dependence of the transmission probabilities on  $\kappa$  for  $N = 195$  without detuning. The transmission probabilities become unity when  $\kappa \simeq 4g$ . The dependence of the transmission probabilities on  $\Delta\omega$  asymptotically changes to the ones shown in Fig. 12(b) when  $N$  becomes sufficiently large. These asymptotic profiles do not depend much on the parity of  $N$  and where the transmission lines are attached as long as they are separated from each other sufficiently. The transmission and the reflection probabil-

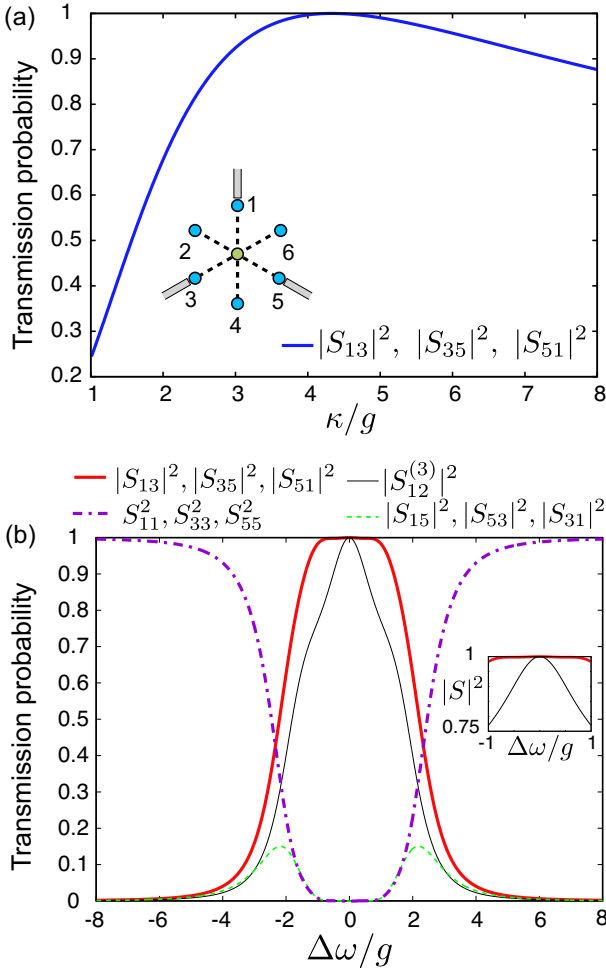


FIG. 11. Circulation properties for the case of  $N = 6$ ,  $\kappa_{1,3,5} = \kappa$ , and  $\kappa_{4,6} = 0$ . (a) Dependence of the forward transmission probabilities ( $|S_{13}|^2$ ,  $|S_{35}|^2$  and  $|S_{51}|^2$ ) on  $\kappa$  for  $\Delta\omega = 0$ . The inset shows the system configuration. (b) Dependence of the forward and backward transmission and reflection probabilities on  $\Delta\omega$  for  $\kappa = 4.328g$ . The black line represents  $|S_{12}^{(3)}|^2$ . The inset is a closeup around  $\Delta\omega/g = 0$ .

ities for  $N = 192$  show the  $\Delta\omega$ -dependence qualitatively similar to the ones for  $N = 195$ , although they are not exhibited here. Note that the system with  $N = 6$  is more robust against the detuning around  $\Delta\omega/g = 0$  than these large  $N$  systems.

The forward transmission probability for large  $N$  system is larger than 0.97 for  $-g < \Delta\omega < g$ , and decreases sharply with the increase of  $|\Delta\omega|$  at  $|\Delta\omega| \sim \pi g$ . The asymptotic value of the full width at half maximum of the forward transmission probability of  $2\pi g$  is attributed to the energy band of the GR cluster, which is from  $-\hbar g\pi$  to  $\hbar g\pi$ . The incoming microwave can enter to the GR cluster and can propagate as a plane wave if its energy is in that range, otherwise it is reflected.

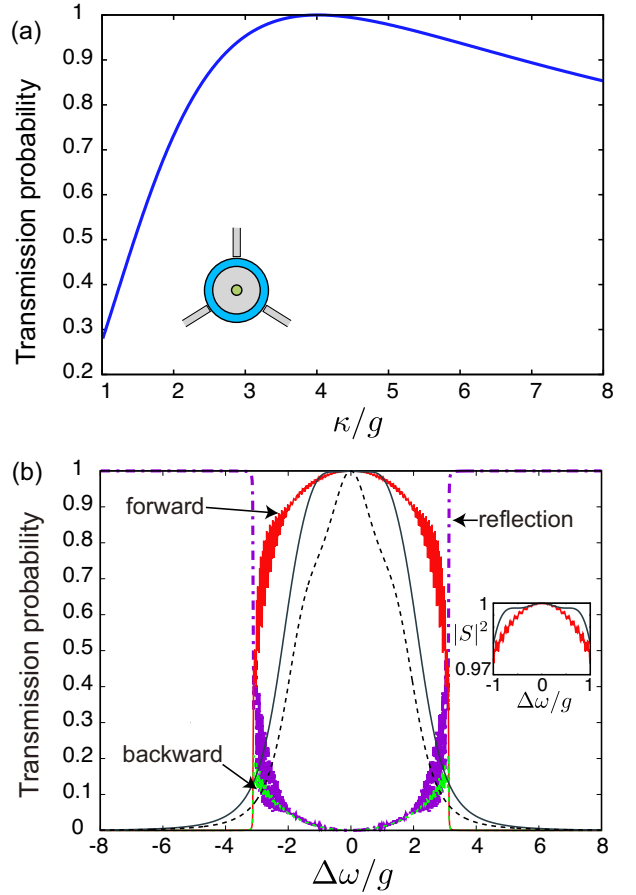


FIG. 12. Circulation properties for the case of  $N = 195$ ,  $\kappa_{1,66,131} = \kappa$ , and  $\kappa_i = 0$  for  $i \neq 1, 66, 131$ . (a) Dependence of the forward transmission probabilities on  $\kappa$  for  $\Delta\omega = 0$ . The inset schematically shows the system configuration for large  $N$ . (b) Dependence of the forward and backward transmission and reflection probabilities on  $\Delta\omega$  for  $\kappa \simeq 4g$ . The transmission and reflection probabilities for  $N = 195$  are indicated by arrows in the panel. The red (gray) solid and the purple (gray) dash-dotted lines are for the forward transmission and the reflection probabilities for  $N = 195$ , respectively. The green (light gray) dashed line, which has the peaks at  $|\Delta\omega/g| \simeq \pi$ , is for the backward transmission probability for  $N = 195$ . The black solid and dashed lines are for the forward transmission probabilities for  $N = 6$  system in Fig. 11(b) and  $N = 3$ , respectively. The right inset is the closeup around  $\Delta\omega/g = 0$ . The upper black line is for  $N = 6$ , and the lower red (gray) line is for  $N = 195$ .

### G. Properties of circulator based on GR hoppings

Here we discuss the general properties of the circulator based on GR hopping with transmission lines A, B and C. As we observed in Sec. IV C, several equalities hold in the transmission probabilities for odd  $N$ . We numerically confirmed that  $S_{AB} = S_{BC} = S_{CA}$ ,  $S_{AC} = S_{CB} = S_{BA}$  and  $S_{AA} = S_{BB} = S_{CC}$  for  $\Delta\omega = 0$  irrespectively of the resonators to which the transmission lines are attached.

The equalities for  $N = 5$  are derived analytically in Appendix D.

On the other hand, these equalities do not generally hold for even  $N$ . However similar equalities hold when the transmission lines are attached in a way that the system is geometrically symmetric against  $2\pi/3$  rotation (see also Appendix D for the  $N = 6$  case). Importantly, the equalities which is desirable for a circulator,  $|S_{AB}| = |S_{BC}| = |S_{CA}|$ , hold for the six-resonator system as seen in Fig. 10(b).

### H. Quantification of circulator performance

To compare the performance of the circulators with different  $N$  quantitatively, we introduce the operating bandwidth  $\Delta\omega_{\text{op}}^{(N)}(P)$  as the range of  $\Delta\omega$ , where the forward transmission probability is larger than the threshold  $P$ . Here, we examine  $\Delta\omega_{\text{op}}^{(N)}(P)$  for  $P = 0.99, 0.9, 0.8$  and  $0.5$  as example. Figure 13 shows  $\Delta\omega_{\text{op}}^{(N)}$  normalized by  $g$  as a function of  $N$ .  $\Delta\omega_{\text{op}}^{(N)}$  for  $N > 3$  is larger than the one for  $N = 3$ .  $\Delta\omega_{\text{op}}^{(6)}$  is the largest for  $P = 0.99$ , and  $\Delta\omega_{\text{op}}^{(7)}$  is the largest for  $P = 0.9, 0.8$  and  $0.5$  in the used system configurations.

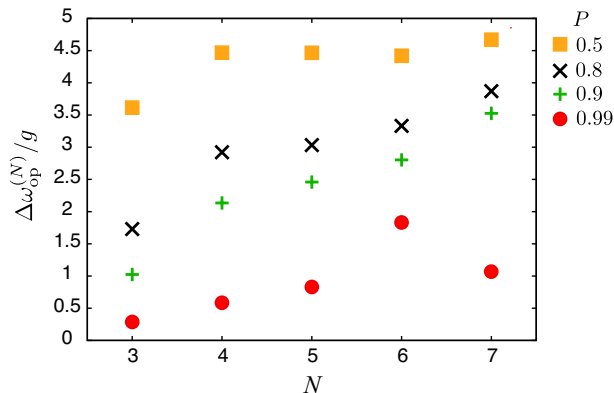


FIG. 13. The dependence of  $\Delta\omega_{\text{op}}^{(N)}$  on  $N$  for  $P = 0.5, 0.8, 0.9$  and  $0.99$ . The results for  $N = 3, 4, 5, 6$  and  $7$  correspond to Figs. 7, 10, 8, 11 and 19, respectively. The circulators for  $N = 4, 5, 7$  have two different values of  $\Delta\omega_{\text{op}}^{(N)}$  corresponding to different input ports respectively. The higher values are shown here. Another values are 28% lower at most than higher ones (not shown).

Some systems with the nearest neighbor hopping can also work as a circulator. In Appendix E, we show that a  $N = 5$  system with the nearest neighbor hopping can work as a circulator, but its performance as a circulator is less than the circulator with GR hopping with  $N > 3$ .

### I. Quantification of directionality

To compare the directionality of the circulators with different  $N$  quantitatively, we examine the directionality parameter defined by [42]

$$d_{AB}(\Delta\omega) \equiv 1 - \frac{|S_{BA}(\Delta\omega)|^2}{|S_{AB}(\Delta\omega)|^2}, \quad (9)$$

where  $|S_{AB}|^2$  and  $|S_{BA}|^2$  are the forward and the backward transmission probabilities, respectively, and  $A$  and  $B$  denote transmission lines.  $d_{AB} = 0$  corresponds to the reciprocal transmission, and  $d_{AB} = 1$  corresponds to the perfect nonreciprocity. Figure 14 shows the dependence of directionality parameter on  $\Delta\omega$  for  $N = 3, 4, 5$  and  $6$ .

Now we introduce the directionality bandwidth  $\Delta\omega_{\text{d}}^{(N)}(P_{\text{d}})$  as the range of  $\Delta\omega$ , where the directionality parameter is the larger than the threshold  $P_{\text{d}}$ . Figure 15 shows the dependence of  $\Delta\omega_{\text{d}}^{(N)}$  on  $N$  for  $P_{\text{d}} = 0.5, 0.8$  and  $0.9$ .  $\Delta\omega_{\text{d}}^{(7)}$  is largest for  $P_{\text{d}} = 0.8$  and  $0.9$ , and  $\Delta\omega_{\text{d}}^{(5)}$  is the largest for  $P_{\text{d}} = 0.5$  in the used system configurations.

### J. Drawback and other possible configurations

The drawback of our scheme is the number of the required couplings between resonators,  $N(N-1)/2$ , increasing with the number  $N$  of resonators. Unwanted crosstalk between resonators and unwanted excitations of the coupler should be avoided. Thus, it becomes experimentally more challenging when  $N$  increases. We discuss the physical realization of our circulator with a concrete circuit model in Appendix G.

In the present article we have mainly studied the systems with small number of resonators  $N$  and with only three transmission lines. Only a part of the possible arrangements of the transmission lines have been examined, although there are many other choices in the arrangement for cases with large  $N$ . The optimized arrangement will be studied for larger  $N$  in an experimentally feasible range elsewhere, and routing microwaves based on other types of long range hopping will be also studied.

### K. Noise analysis

We study the effect of noise by taking into account internal dissipation of resonators. The internal dissipation is modeled by a fictional transmission line attached to each resonator (see Appendix H for details).

The output noise spectral density [30, 45] of resonator  $m$  is represented as

$$P_m^{(\text{out})}(\Delta\omega) = \sum_{n,\alpha} \left\{ |S_{nm}^{(\alpha)}(\Delta\omega)|^2 \left( \bar{n}_n^{(\alpha)} + \frac{1}{2} \right) \right\}, \quad (10)$$

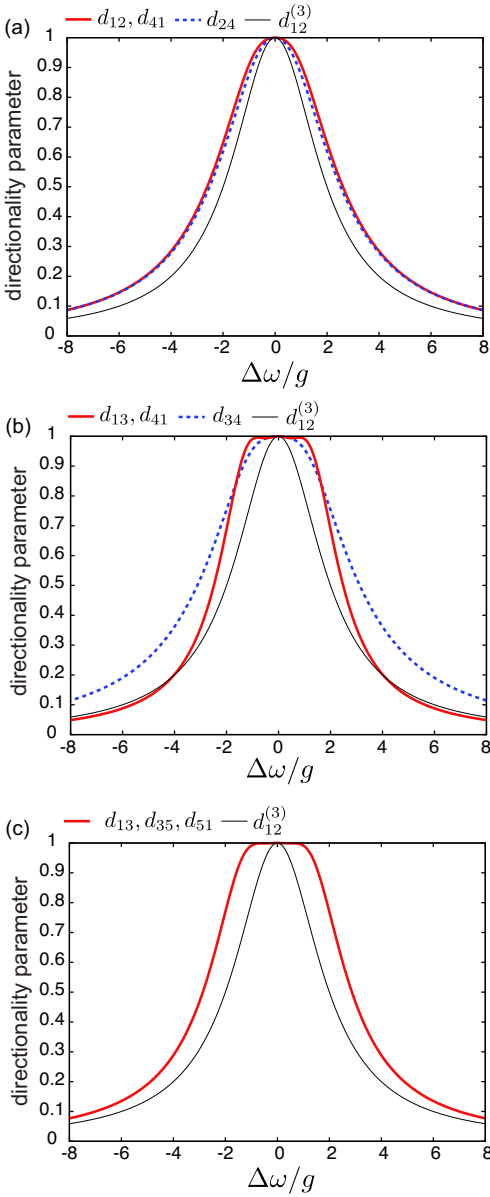


FIG. 14. The dependence of directionality parameter on  $\Delta\omega$  for  $N = 4$  (a),  $N = 5$  (b) and  $N = 6$  (c). The thin black line is for  $N = 3$ . The used system configurations and the parameters for  $N = 3, 4, 5$  and  $6$  are the same as Figs. 7, 10, 8 and 11, respectively.

where  $\alpha$  runs over  $b$  and  $c$ , and

$$\begin{aligned} S_{nm}^{(b)} &= \delta_{m,n} - \sqrt{\kappa_m \kappa_n} [\mathcal{G}^{-1}]_{m,n}, \\ S_{nm}^{(c)} &= -\sqrt{\kappa_m \kappa_n^{(\text{int})}} [\mathcal{G}^{-1}]_{m,n}. \end{aligned} \quad (11)$$

$\mathcal{G}$  is given in Eq. (H4).  $\kappa_m^{(\text{int})}$  is the internal decay rate of resonator  $m$ , and  $\Delta\omega$  is the detuning.  $\bar{n}_m^{(b/c)}$  is the thermal equilibrium occupation number defined by Eq. (H14) with the temperature of the actual or fictional transmission line  $T_m^{(b/c)}$  attached to resonator  $m$ .

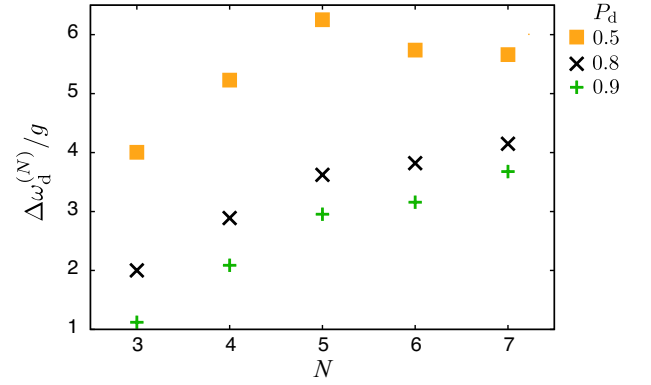


FIG. 15. The dependence of  $\Delta\omega_d^{(N)}$  on  $N$  for  $P_d = 0.5, 0.8$  and  $0.9$ . The used system configurations and the parameters are the same as Fig. 13. The circulators for  $N = 4, 5, 7$  have two different values of  $\Delta\omega_d^{(N)}$  corresponding to different input ports respectively. The higher values are shown here. Another values are 20% lower at most than higher ones (not shown).

As an example we consider the case where the thermal noise from port 1 is dominant, that is,  $\bar{n}_1^{(b)}$  is finite and other thermal equilibrium occupation numbers are zero. Figure 16 shows the dependence of  $P_m^{(\text{out})}(\Delta\omega)$  in Eq. (10) on  $\Delta\omega$  for  $\kappa_m^{(\text{int})} = 0.02g$  for  $N = 3$  and  $N = 6$ .  $\kappa_m^{(\text{int})} = 0.02g$  corresponds to the cooperativity of 100, where the cooperativity is defined as  $C_m = 4g^2/(\kappa_m \kappa_m^{(\text{int})})$  for  $N = 3$ . The profile of  $P_m^{(\text{out})}(\Delta\omega)$  is similar to that of the amplitude of the  $S$ -matrix elements although there is the offset of 0.5 corresponding to the zero point fluctuation.

In the case where  $\bar{n}_m \ll 1$ ,  $P_m^{(\text{out})}(\Delta\omega)$  becomes 0.5 because of the unitarity of the  $S$ -matrix of the system including the fictitious transmission lines.

The input noise is not amplified by our device with the gain of unity. However the noise,

$$P_m^{\text{add}} = \sum_n \left\{ |S_{nm}^{(c)}(\Delta\omega)|^2 \bar{n}_n^{(c)} \right\}, \quad (12)$$

which is included in Eq. (10) and corresponding to the internal loss of each resonator, is added when the microwaves pass through the device. The added noise is much smaller than input noise if  $\kappa_n^{(\text{int})} \ll \kappa_n$  because  $S_{mn}^{(c)}$  is proportional to  $(\kappa_n^{(\text{int})})^{1/2}$  whereas  $S_{mn}^{(b)}$  is proportional to  $\kappa_n^{1/2}$  as shown in Eq. (11).

### 1. Effect to $S$ -matrix

We examine the effect of  $\kappa_m^{(\text{int})}$  to the  $S$ -matrix. Figure 17(a) and 17(b) show the dependence of the forward and backward transmission probabilities and reflection probability on  $\Delta\omega$  for  $N = 3$  and  $6$ . The forward transmission probability decreases with the increase of  $\kappa_m^{(\text{int})}$  as seen in the case with  $\kappa_m^{(\text{int})} = 0.02g$  due to the internal

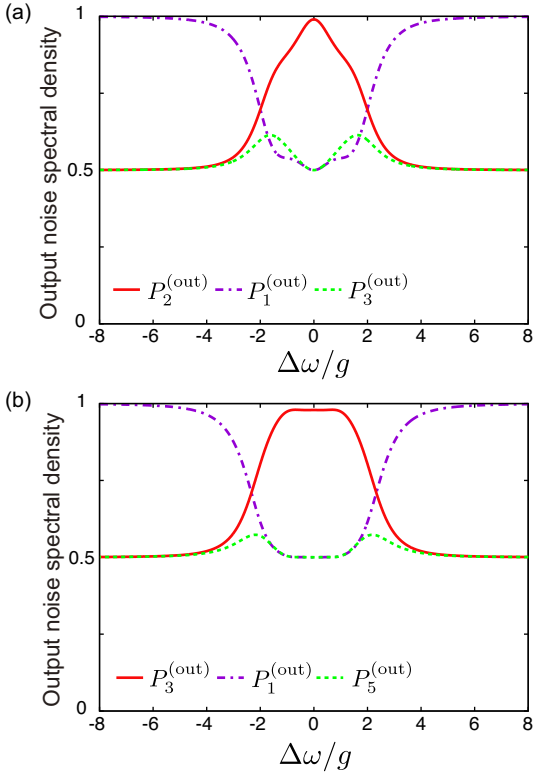


FIG. 16. Dependence of  $P_m^{(out)}(\Delta\omega)$  in Eq. (10) on  $\Delta\omega$  for  $\kappa_m^{(int)} = 0.02g$  for  $N = 3$  (a) and  $N = 6$  (b). The solid lines correspond to the forward transmission of the noise, while the dashed and the dotted lines correspond to the backward transmission and reflection, respectively. The thermal equilibrium occupation numbers used are  $\bar{n}_1^{(b)} = 0.5$ ,  $\bar{n}_n^{(b)} = 0$  for  $n \neq 1$  and  $\bar{n}_n^{(c)} = 0$ . The system configurations and  $\kappa_m$  are the same as Fig. 7 and Fig. 11, respectively.

loss of the resonators, while the decrease of the forward transmission probability is negligible for  $\kappa_m^{(int)} = 0.002g$  because the internal loss is sufficiently small. The backward transmission probability and reflection probability are approximately the same as the ones for  $\kappa_m^{(int)} = 0$  in the used values of  $\kappa_m^{(int)}$ .

Figure 18 shows the dependence of the forward transmission probabilities on  $\Delta\omega$  for  $\kappa_m^{(int)} = 0.02g$  and  $N = 3, 4, 5$  and  $6$ . It is seen that the forward transmission probabilities for  $N > 3$  is higher than that of  $N = 3$  in a wide range of  $\Delta\omega$ . However  $|S_{24}|^2$  for  $N = 4$  in Fig. 18(a),  $|S_{13,41}|^2$  for  $N = 5$  in Fig. 18(b) and the forward transmission probability for  $N = 6$  in Fig. 18(c) are slightly lower than  $|S_{13}^{(3)}|^2$  around  $\Delta\omega = 0$ , although  $|S_{12}|^2$  and  $|S_{41}|^2$  for  $N = 4$  and  $|S_{34}|^2$  for  $N = 5$  are higher than  $|S_{13}^{(3)}|^2$  also at  $\Delta\omega = 0$ .

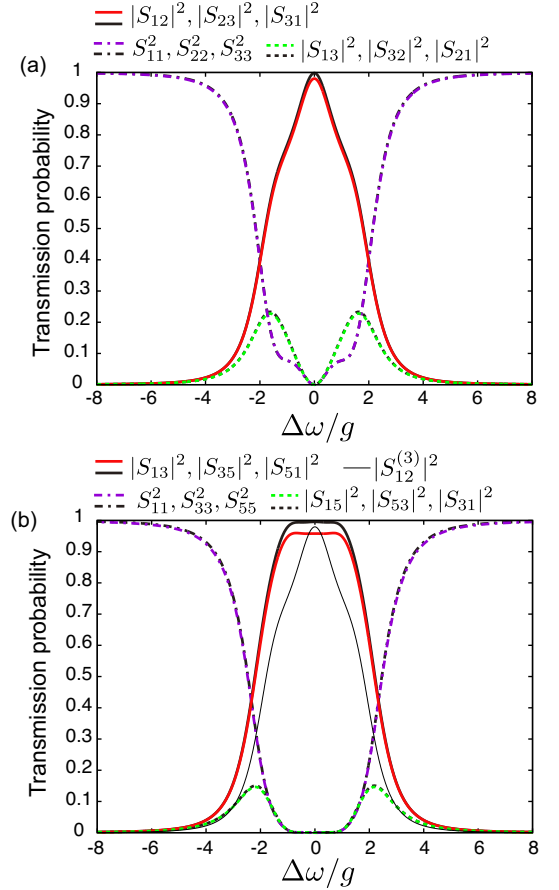


FIG. 17. Dependence of the forward and backward transmission probabilities and reflection probability on  $\Delta\omega$  for  $\kappa_m^{(int)} = 0.02g, 0.002g$  for  $N = 3$  (a) and  $N = 6$  (b). The system configurations and  $\kappa_m$  are the same as Fig. 7 and Fig. 11, respectively. The data for  $\kappa_m^{(int)} = 0.02g$  and  $0.002g$  are represented by colored (gray) and black lines, respectively. The thin line in panel (b) shows the forward transmission probability for  $N = 3$  for  $\kappa_m^{(int)} = 0.02g$ .

## V. CONCLUSION AND DISCUSSION

We have proposed an on-chip microwave circulator based on the Gebhard-Ruckenstein (GR) hopping. The linear energy dispersion of the GR cluster gives rise to a chiral propagation of a microwave, and thus can work as a circulator when transmission lines are attached. Our circulators composed of more than three resonators can have a wider operating bandwidth than that composed of three resonators. The robustness of the routing efficiency against the inhomogeneity in the system parameters has also been examined. Although in this manuscript we have focused on gainless circulation of photon, application of this system to directional amplification will be studied elsewhere.

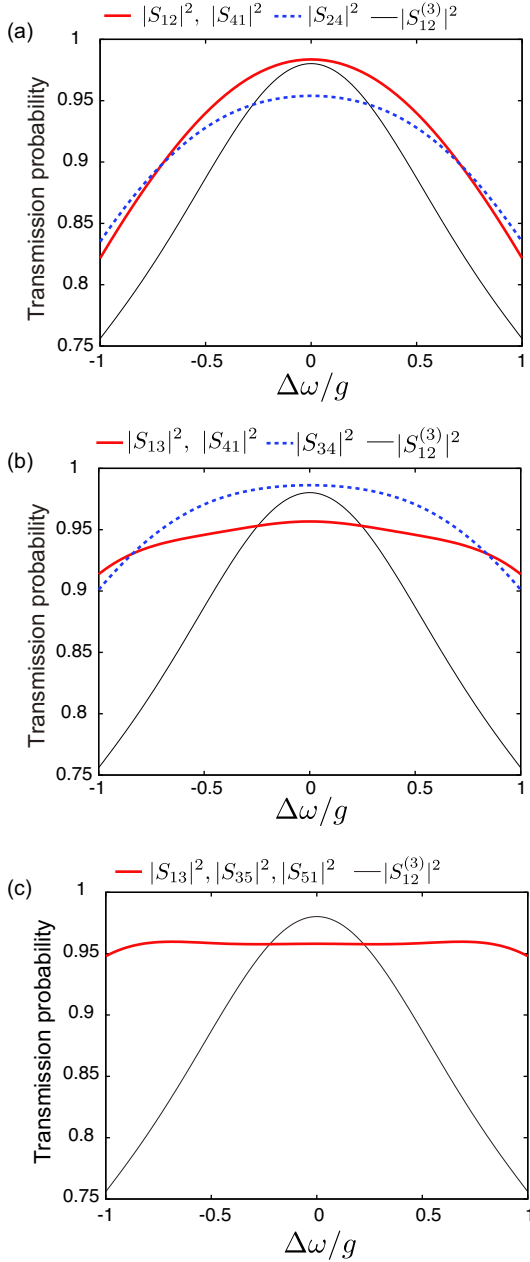


FIG. 18. Dependence of the forward transmission probabilities on  $\Delta\omega$  for  $\kappa_m^{(\text{int})} = 0.02g$  for  $N = 4$  (a),  $N = 5$  (b),  $N = 6$  (c). The system configurations and  $\kappa_m$  are the same as Figs. 10, 8 and 11, respectively. The black thin line represents  $|S_{12}^{(3)}|^2$ .

## ACKNOWLEDGMENTS

We acknowledge the supports from JST ERATO (Grant No. JPMJER1601) and JSPS KAKENHI (Grant No. 16K05497 and No. 18K03486).

## Appendix A: Chiral propagation induced by linear dispersion

We show that the linear dispersion results in the chiral propagation of a microwave photon in an isolated GR cluster. We consider a single photon state of the GR cluster. A single photon state can be represented as a superposition of the energy eigenstates  $|\nu\rangle$  in Eq. (5) as

$$|\Psi(t)\rangle = \sum_{\nu} \varphi_{\nu} e^{-i\eta_0 k_{\nu} t} |\nu\rangle, \quad (\text{A1})$$

where the coefficients  $\varphi_{\nu}$  are complex constants. Thus, the wave function,  $\Psi(m, t) \equiv \langle m | \Psi(t) \rangle$ , is represented as

$$\Psi(m, t) = \frac{1}{\sqrt{N}} \sum_{\nu} \varphi_{\nu} \exp[ik_{\nu}(m - \eta_0 t)]. \quad (\text{A2})$$

The expectation value of photon number at site  $m$  is given by

$$|\Psi(m, t)|^2 = \sum_{\nu\nu'} \frac{\varphi_{\nu'}^* \varphi_{\nu}}{N} e^{i(k_{\nu} - k_{\nu'})(m - \eta_0 t)}. \quad (\text{A3})$$

Using  $r_{\nu, \nu'}, \theta_{\nu, \nu'} \in R$  defined as

$$r_{\nu, \nu'} e^{i\theta_{\nu, \nu'}} = \frac{\varphi_{\nu'}^* \varphi_{\nu}}{N}, \quad (\text{A4})$$

$|\Psi(m, t)|^2$  in Eq. (A3) is rewritten as

$$|\Psi(m, t)|^2 = 1 + \sum_{\nu' > \nu} r_{\nu, \nu'} \cos[(k_{\nu} - k_{\nu'})(m - \eta_0 t) + \theta_{\nu, \nu'}]. \quad (\text{A5})$$

Obviously the envelope of  $|\Psi(m, t)|^2$  propagates in the same direction with velocity  $a_L \eta_0$ , where  $a_L$  is the distance between neighboring sites.

## Appendix B: Derivation of $S$ -matrix

We derive the  $S$ -matrix of the system, which is described by the Hamiltonian of Eq. (6) [43,44]. The Heisenberg equation of motion of  $b_{m,k}$  is represented as

$$\frac{d}{dt} b_{m,k}(t) = -ivkb_{m,k}(t) - i\sqrt{\frac{v\kappa_m}{2\pi}} a_m(t). \quad (\text{B1})$$

We define the real-space representation  $\tilde{b}_{m,r}$  of the transmission line field as

$$\tilde{b}_{m,r} = \frac{1}{\sqrt{2\pi}} \int_{-\infty}^{\infty} dk e^{ikr} b_{m,k}. \quad (\text{B2})$$

Tildes are used to distinguish the operator in  $k$ -space representation from the one in  $r$ -space representation in this section. In this representation, the field interacts with resonator at  $r = 0$ , and the  $r < 0$  ( $r > 0$ ) region corresponds to the incoming (outgoing) field. The input and output field operators of the transmission line field

are defined by

$$\begin{aligned}\tilde{b}_{m,r}^{(\text{in})}(t) &= \tilde{b}_{m,-r}(t), \\ \tilde{b}_{m,r}^{(\text{out})}(t) &= \tilde{b}_{m,r}(t),\end{aligned}\quad (\text{B3})$$

respectively, where  $r > 0$ . Using Eqs. (B1) and (B3), the input-output relation is derived as [43, 44]

$$\tilde{b}_{m,r}^{(\text{out})}(t) = \tilde{b}_{m,vt-r}^{(\text{in})}(0) - i\sqrt{\frac{\kappa_m}{v}}\theta(r)\theta(vt-r)a_m(t-r/v).\quad (\text{B4})$$

The Heisenberg equation of motion of  $a_m$  is represented as

$$\begin{aligned}\frac{d}{dt}a_m &= \left(-i\omega_m - \frac{\kappa_m}{2}\right)a_m - i\sum_{n(\neq m)}g_{m,n}(t)a_n \\ &\quad - i\sqrt{v\kappa_m}\tilde{b}_{m,vt}^{(\text{in})}.\end{aligned}\quad (\text{B5})$$

So far we discussed the operator equations. Here we assume that an input microwave is applied from the transmission line attached to the  $p$ -th resonator. We consider a continuous mode version of a coherent state:

$$|\Psi_i\rangle = \mathcal{N} \exp\left[\int_0^\infty dr E_{\text{in}}(r)(\tilde{b}_{p,r}^{(\text{in})})^\dagger\right]|0\rangle, \quad (\text{B6})$$

with the overall vacuum state  $|0\rangle$  and a normalization constant  $\mathcal{N}$ . Considering that the input wave propagates in the negative  $r$  direction,  $E_{\text{in}}(r)$  represents the input microwave at the initial moment as given by

$$E_{\text{in}}(r) = Ee^{-i\omega_{\text{in}}r/v}, \quad (\text{B7})$$

where  $E$  and  $\omega_{\text{in}}$  are the amplitude and the angular frequency of the incident microwave, respectively. We assume that at the initial moment the resonators and the transmission lines except for the input one are unexcited, and the input microwave has not arrived at resonator  $p$  yet.  $|\Psi_i\rangle$  is in a coherent state and therefore an eigenstate of the initial field operator  $\tilde{b}_{p,r}(0)$ . It is confirmed that

$$\tilde{b}_{m,vt}^{(\text{in})}|\Psi_i\rangle = E_{\text{in}}(vt)\delta_{m,p}|\Psi_i\rangle = Ee^{-i\omega_{\text{in}}t}\delta_{m,p}|\Psi_i\rangle \quad (\text{B8})$$

using Eqs. (B3) and (B6).

We rewrite Eq. (B5) as

$$\begin{aligned}\frac{d}{dt}A_m &= \left(i\Delta\omega - \frac{\kappa_m}{2}\right)A_m - i\sum_{n(\neq m)}g_{m,n}(t)e^{i(\omega_m - \omega_n)t}A_n \\ &\quad - i\sqrt{v\kappa_m}\tilde{b}_{m,vt}^{(\text{in})}e^{i(\omega_m + \Delta\omega)t}\end{aligned}\quad (\text{B9})$$

with  $A_m$  defined by

$$A_m(t) = e^{i(\omega_m + \Delta\omega)t}a_m(t), \quad (\text{B10})$$

where  $\Delta\omega$  is the detuning of the incident microwave with angular frequency  $\omega_{\text{in}}$ , that is,  $\omega_{\text{in}} = \omega_p + \Delta\omega$ . Using Eqs. (2) and (B9) and the rotating wave approximation,

we obtain

$$\begin{aligned}\frac{d}{dt}A_m &= \left(i\Delta\omega - \frac{\kappa_m}{2}\right)A_m - i\sum_{n(\neq m)}\bar{g}_{m,n}e^{-i\theta_{m,n}}A_n \\ &\quad - i\sqrt{v\kappa_m}\tilde{b}_{m,vt}^{(\text{in})}e^{i(\omega_m + \Delta\omega)t}.\end{aligned}\quad (\text{B11})$$

Taking the expectation value of Eq. (B11) with respect to  $|\Psi_i\rangle$  we obtain

$$\begin{aligned}\frac{d}{dt}\langle A_m \rangle &= \left(i\Delta\omega - \frac{\kappa_m}{2}\right)\langle A_m \rangle - i\sum_{n(\neq m)}\bar{g}_{m,n}e^{-i\theta_{m,n}}\langle A_n \rangle \\ &\quad - i\sqrt{v\kappa_m}E\delta_{m,p}.\end{aligned}\quad (\text{B12})$$

To obtain the stationary solution in the rotating frame we put  $d\langle A_m \rangle/dt = 0$ . Then Eq. (B12) is rewritten in the matrix form as

$$\mathcal{G}\langle \vec{A} \rangle = -i\sqrt{v\kappa_p}E\vec{\phi}_p, \quad (\text{B13})$$

where the  $(m, n)$  element of matrix  $\mathcal{G}$  is given by

$$\mathcal{G}_{m,n} = \begin{cases} \kappa_m/2 - i\Delta\omega & (n = m) \\ i\bar{g}_{m,n}e^{-i\theta_{m,n}} & (n \neq m), \end{cases} \quad (\text{B14})$$

and

$$\langle \vec{A} \rangle = (\langle A_1 \rangle, \dots, \langle A_N \rangle), \quad (\text{B15})$$

and the  $p$ -th component of  $\vec{\phi}_p$  is 1, while the others are 0. Then  $\langle \vec{A} \rangle$  is written with the inverse of matrix  $\mathcal{G}$  as

$$\langle \vec{A} \rangle = -i\sqrt{v\kappa_p}E\mathcal{G}^{-1}\vec{\phi}_p. \quad (\text{B16})$$

We multiply Eq. (B4) by  $e^{i(\omega_m + \Delta\omega)t}$  with  $r = +0$  and take the expectation value with respect to  $|\Psi_i\rangle$  to obtain

$$\langle \tilde{B}_{m,+0}^{(\text{out})}(t) \rangle = \langle \tilde{B}_{m,vt}^{(\text{in})} \rangle - i\sqrt{\frac{\kappa_m}{v}}\langle A_m(t) \rangle, \quad (\text{B17})$$

where

$$\begin{aligned}\tilde{B}_{m,+0}^{(\text{out})}(t) &= \tilde{b}_{m,+0}^{(\text{out})}(t)e^{i(\omega_m + \Delta\omega)t} \\ \tilde{B}_{m,vt}^{(\text{in})} &= \tilde{b}_{m,vt}^{(\text{in})}e^{i(\omega_m + \Delta\omega)t}.\end{aligned}\quad (\text{B18})$$

Using the stationary solution of  $\langle A_m \rangle$  given by Eq. (B16), the stationary solution of  $\langle \tilde{B}_{m,+0}^{(\text{out})} \rangle$  is given by

$$\langle \tilde{B}_{m,+0}^{(\text{out})} \rangle = \langle \tilde{B}_{m,vt}^{(\text{in})} \rangle - i\sqrt{\frac{\kappa_m}{v}}\langle A_m \rangle, \quad (\text{B19})$$

where

$$\langle \tilde{B}_{m,vt}^{(\text{in})} \rangle = \delta_{m,p}E, \quad (\text{B20})$$

because of Eq. (B8). The elements of  $S$ -matrix are defined by

$$S_{p,m} = \frac{\langle \tilde{b}_{m,+0}(t) \rangle}{\langle \tilde{b}_{p,-0}(t) \rangle}. \quad (\text{B21})$$

With the use of Eqs. (B16), (B18), (B19), (B20), (B21) and  $\tilde{b}_{m,vt}^{(\text{in})}(0) = \tilde{b}_{m,+0}^{(\text{in})}(t)$ , the  $S$ -matrix element is given as

$$\begin{aligned} S_{p,m} &= \delta_{p,m} - \sqrt{\kappa_p \kappa_m} [\mathcal{G}^{-1} \vec{\phi}_p]_m, \\ &= \delta_{p,m} - \sqrt{\kappa_p \kappa_m} [\mathcal{G}^{-1}]_{m,p}, \end{aligned} \quad (\text{B22})$$

where  $[\mathcal{G}^{-1} \vec{\phi}_p]_m$  denotes the  $m$ -th component of vector,  $\mathcal{G}^{-1} \vec{\phi}_p$ . This is identical to  $[\mathcal{G}^{-1}]_{m,p}$ , since the  $p$ -th component of  $\vec{\phi}_p$  is 1 and the others are 0.

### Appendix C: Results for seven-resonator system

Figure 19(a) shows the dependence of the forward transmission probabilities on  $\kappa$  for  $N = 7$ . The transmission lines are coupled to resonators 1, 3 and 6 as shown in the inset. It is numerically confirmed that the forward transmission probabilities,  $|S_{13}|^2$ ,  $|S_{36}|^2$  and  $|S_{61}|^2$ , are identical in spite of the absence of the three fold rotational symmetry and become unity at  $\kappa \simeq 4.45g$ . We also analytically confirmed the equalities of the forward transmission probabilities in the same manner as Appendix D. Figure 19(b) and 19(c) show the dependence of the forward transmission probabilities on detuning  $\Delta\omega$  for  $\kappa = 4.45g$ . The transmission probabilities for  $N = 7$  are generally higher than those for  $N = 5$  in Fig. 8(b) in a wide range of  $\Delta\omega$ . The profile of the transmission probabilities for  $N = 7$  is close to a rectangular shape compared to the one for  $N = 3$ . The backward transmission and the reflection probabilities for  $N = 7$  show the  $\Delta\omega$ -dependence qualitatively similar to the ones for  $N = 5$  in Fig. 8(b), although they are not exhibited here. The directionality parameter in Eq. (9) is shown in Fig. 20. It is seen that the system with  $N = 7$  has robust directionality compared to the system with  $N = 3$ .

### Appendix D: Equalities between $S$ -matrix elements

We analytically show the equalities between the  $S$ -matrix elements, which are numerically confirmed in Secs. IVC and IVE. We consider the matrix  $\mathcal{G}$  in Eq. (B13) for the system with  $N = 5$  depicted in Fig. 6. The matrix  $\mathcal{G}$  has the form as

$$\mathcal{G} = \begin{pmatrix} x & a & b & -b & -a \\ -a & 0 & a & b & -b \\ -b & -a & x & a & b \\ b & -b & -a & x & a \\ a & b & -b & -a & 0 \end{pmatrix}, \quad (\text{D1})$$

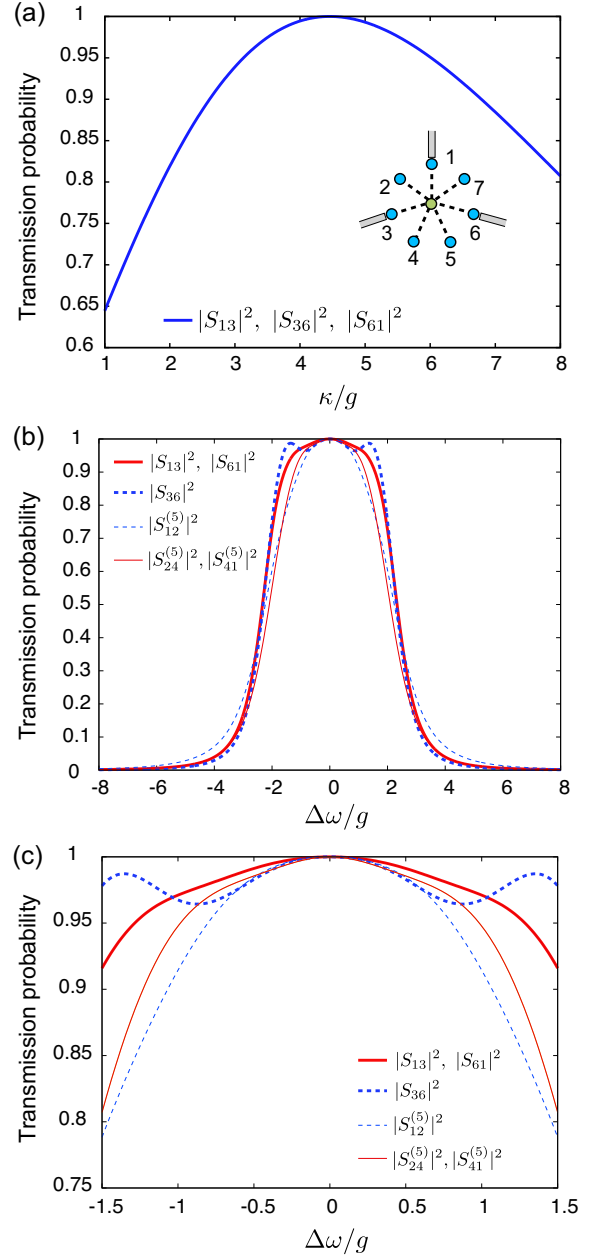


FIG. 19. Circulation properties for the case of  $N = 7$ ,  $\kappa_{1,3,6} = \kappa$ , and  $\kappa_{2,4,5,7} = 0$ . (a) Dependence of the forward transmission probabilities on the coupling to transmission line  $\kappa$  for  $\Delta\omega = 0$ . The inset shows the system configuration. (b) Dependence of the forward transmission probabilities on detuning  $\Delta\omega$  for  $\kappa = 4.45g$ . The thin lines correspond to the system with  $N = 5$  in Fig. 8. (c) Closeup of (b) around  $\Delta\omega/g = 0$ .

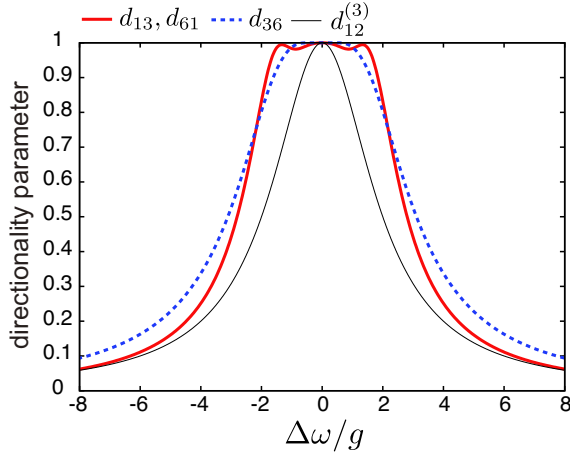


FIG. 20. The dependence of directionality parameter in Eq. (9) on  $\Delta\omega$  for  $N = 7$ . The used parameters and the configuration are the same as Fig. 19. The thin black line is for the system with  $N = 3$  shown in Fig. 7.

with real constants  $x$ ,  $a$  and  $b$  when  $\Delta\omega = 0$ . The matrix elements of  $\mathcal{G}^{-1}$  are represented as

$$\begin{aligned} [\mathcal{G}^{-1}]_{31/43/14} &= \frac{A_5 + B_5 x}{3A_5 x + b^2 x^3}, \\ [\mathcal{G}^{-1}]_{41/34/13} &= \frac{A_5 - B_5 x}{3A_5 x + b^2 x^3}, \\ [\mathcal{G}^{-1}]_{11/33/44} &= \frac{A_5 + b^2 x^2}{3A_5 x + b^2 x^3} \end{aligned} \quad (\text{D2})$$

with

$$\begin{aligned} A_5 &= a^4 - 2a^3 b - a^2 b^2 + 2ab^3 + b^4, \\ B_5 &= -a^2 b + ab^2 + b^3. \end{aligned} \quad (\text{D3})$$

From Eq. (7), we obtain the following equalities between the  $S$ -matrix elements:

$$\begin{aligned} S_{13} &= S_{34} = S_{41}, \\ S_{14} &= S_{43} = S_{31}, \\ S_{11} &= S_{33} = S_{44}. \end{aligned} \quad (\text{D4})$$

it is confirmed analytically that the same equalities hold in the system with  $N = 7$ .

Now we consider the case with  $N = 6$  depicted in Fig. 10(b). Because matrix  $\mathcal{G}$  has the following form:

$$\mathcal{G} = \begin{pmatrix} x & a & b & c & b & a \\ -a & 0 & a & b & c & b \\ -b & -a & x & a & b & c \\ -c & -b & -a & 0 & a & b \\ -b & -c & -b & -a & x & a \\ -a & -b & -c & -b & -a & 0 \end{pmatrix}, \quad (\text{D5})$$

for the case  $\Delta\omega = 0$ , we have the equalities relevant to

$S$ -matrix such as

$$\begin{aligned} [\mathcal{G}^{-1}]_{31/53} &= -[\mathcal{G}^{-1}]_{15}, \\ [\mathcal{G}^{-1}]_{35/13} &= -[\mathcal{G}^{-1}]_{51}, \\ [\mathcal{G}^{-1}]_{11} &= [\mathcal{G}^{-1}]_{33} = [\mathcal{G}^{-1}]_{55}. \end{aligned} \quad (\text{D6})$$

From these equalities, we have

$$\begin{aligned} S_{13} &= S_{35} = -S_{51}, \\ -S_{15} &= S_{53} = S_{31}, \\ S_{11} &= S_{33} = S_{55}. \end{aligned} \quad (\text{D7})$$

## Appendix E: Nearest neighbor hopping

Some systems with the nearest neighbor hopping can work as a circulator. Here we examine a system with  $N = 5$  and show that it can work as a circulator. However its performance as a circulator is similar to the one with  $N = 3$  and is less than the circulator with GR hopping with  $N > 3$  as explained below. (We do not intend to insist with this result that any systems with the nearest neighbor hopping have lower performance than the circulator with GR hopping.)

Hamiltonian of the resonator part is represented as

$$\mathcal{H}_{\text{cluster}} = \hbar g \sum_{m=1}^5 \left( e^{i\theta} a_{m+1}^\dagger a_m + h.c. \right), \quad (\text{E1})$$

where  $g$ ,  $\theta \in R$ , and the subscripts are modulo 5. The interactions between the transmission lines and the resonator modes is modeled by  $\mathcal{H}_{\text{damp}}$  in Eq. (6).

We consider the case that transmission lines are attached to resonator 1, 2 and 5 with  $\kappa_{1,2,5} = 2g$  and  $\kappa_{3,4} = 0$ , where  $\kappa_{1,2,5}$  was optimized so that the forward transmission probabilities reaches unity. Figure 21(a) shows the dependence of the forward and backward transmission probabilities on detuning  $\Delta\omega$  for  $\theta = \pi/10$  and  $\pi/8$ . The intensity of the  $S$ -matrix elements for  $\theta = \pi/10$  are the same as the system with  $N = 3$  in Fig. 7, and  $|S_{12}|$  corresponding to the forward transmission is given by

$$|S_{12}| = \left| \frac{4 - 2i\Delta\omega}{4 - 6i\Delta\omega - 3\Delta\omega + i\Delta\omega^3} \right|. \quad (\text{E2})$$

On the other hand the peak of the forward transmission probability for  $\theta = \pi/8$  is shifted from  $\Delta\omega = 0$ . Figure 21(b) shows  $|S_{21}|^2 - |S_{12}|^2$  as a function of  $\Delta\omega$  and  $\theta$ .  $\Delta\omega_{\text{op}}^{(5)}$  (0.99) defined in Sec.IV H is 0.286 and 0.234 for  $\theta = \pi/10$  and  $\pi/8$ , respectively. These values are lower than those of the circulator with the GR hopping with  $N > 3$  shown in Fig. 13. In this sense, the performance of this system is lower than the circulator with GR hopping.

The forward and backward transmission probabilities are the same for the system with transmission lines attached to resonators 1, 3 and 4. Thus, it does not work as a circulator.

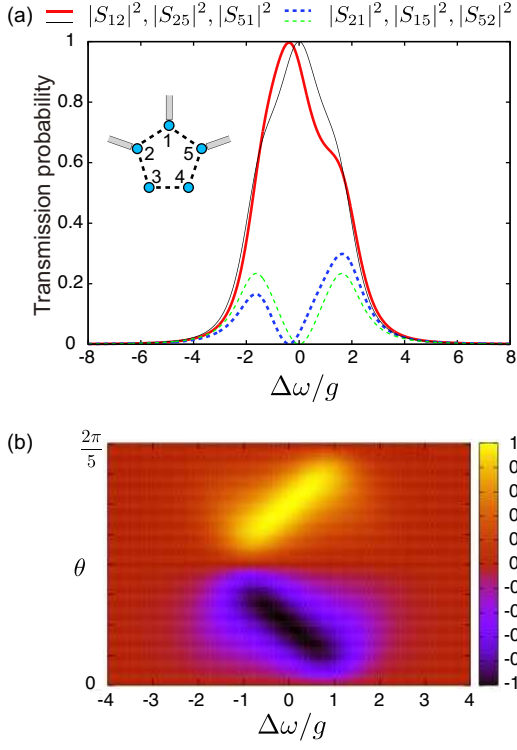


FIG. 21. (a) Dependence of the forward and backward transmission probabilities on detuning  $\Delta\omega$  for  $\kappa_{1,2,5} = 2g$ . The thin lines correspond to the case with  $\theta = \pi/10$ , and thick lines correspond to  $\theta = \pi/8$ . The inset shows the system configuration. (b)  $|S_{21}|^2 - |S_{12}|^2$  as function of  $\Delta\omega$  and  $\theta$ .

### Appendix F: Effects of parameter fluctuations

Here, we observe the effects of fluctuations of the system parameters. To observe the effects of fluctuation in  $\kappa$ , we replace  $\kappa_1$  and  $\kappa_3$  with  $\lambda_{\kappa 1}\kappa_1$  and  $\lambda_{\kappa 3}\kappa_3$ , respectively, for the six-resonator system discussed in Sec. IV E. Figure 22(a) shows the dependence of  $|S_{13}|^2$  on  $\lambda_{\kappa 1}$  and  $\lambda_{\kappa 3}$ .  $|S_{13}|^2$  is approximately 0.93 when  $\kappa_1$  and  $\kappa_3$  have 30% of inhomogeneity. Transmission probabilities  $|S_{35}|^2$  and  $|S_{51}|^2$  (not shown) are higher than 0.965 in the same range of  $\lambda_{\kappa 1}$  and  $\lambda_{\kappa 3}$ .

To observe the effects of the fluctuation in  $g$ , we make the following replacements:  $\bar{g}_{13/31} \rightarrow \lambda_{g13}\bar{g}_{13/31}$  and  $\bar{g}_{35/53} \rightarrow \lambda_{g35}\bar{g}_{35/53}$ . Figure 22(b) shows the dependence of  $|S_{13}|^2$  on  $\lambda_{g13}$  and  $\lambda_{g35}$ .  $|S_{13}|^2$  is approximately 0.93 when the coupling strengths have 30% of inhomogeneity. Transmission probability  $|S_{35}|^2$  is higher than 0.99 and  $|S_{51}|^2$  is higher than 0.93 in the same range of  $\lambda_{g13}$  and  $\lambda_{g35}$  (not shown).

Finally, to observe the effects of the fluctuation in the phase of  $g$ , we replace  $\bar{g}_{13}$  and  $\bar{g}_{35}$  with  $e^{i\theta_1}\bar{g}_{13}$ , and  $e^{i\theta_2}\bar{g}_{35}$ . Figure 22(c) shows the dependence of  $|S_{13}|^2$  on  $\theta_1$  and  $\theta_2$ . Transmission probability  $|S_{35}|^2$  is higher than 0.96 and  $|S_{51}|^2 = |S_{13}|^2$  in the same range of  $\theta_1$  and  $\theta_2$ , although they are not shown here. It is seen that  $|S_{13}|^2$  is

sensitive to  $\theta_1$  compared to  $\theta_2$ .

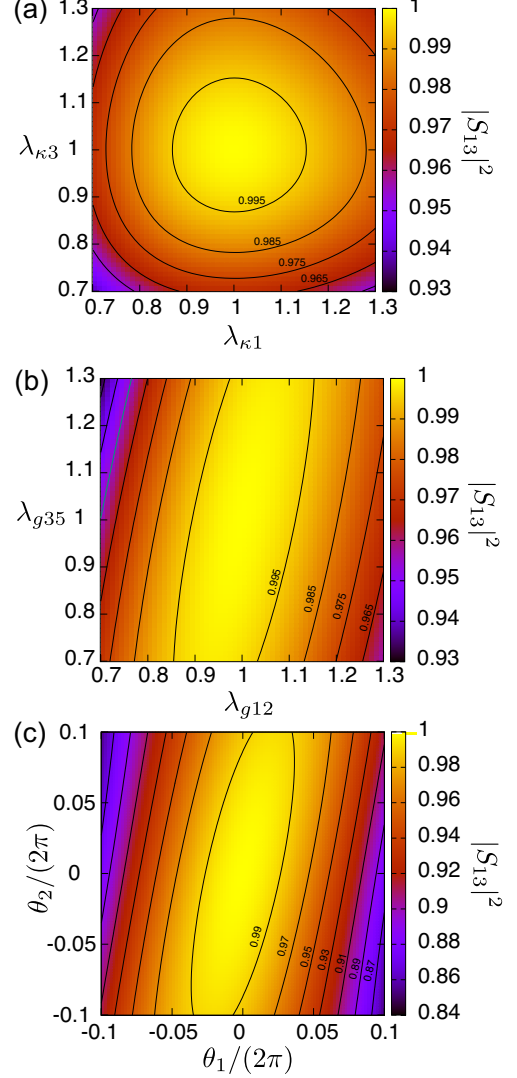


FIG. 22. Effects of the fluctuations in the system parameters. The system with  $N = 6$  in Fig. 10(c) is investigated. Dependence of  $|S_{13}|^2$  on (a)  $\lambda_{\kappa 1}$  and  $\lambda_{\kappa 3}$ , (b)  $\lambda_{g13}$  and  $\lambda_{g35}$ , (c)  $\theta_1$  and  $\theta_2$ . The values next to the contour lines indicate the values of  $|S_{13}|^2$ .

### Appendix G: Physical realization

In this section we discuss the physical realization of our circulator with a concrete circuit model with  $N = 5$ . Figure 23 shows a circuit system of a possible physical realization of the circulator. The system is composed of a Josephson ring, resonators and transmission lines. The Josephson ring works as the coupler depicted in Fig. 6. A magnetic flux,  $\Phi$ , is penetrating the Josephson ring.

We derive an effective photon Hamiltonian for the system depicted in Fig.23 in a manner analogous to Ref.16.

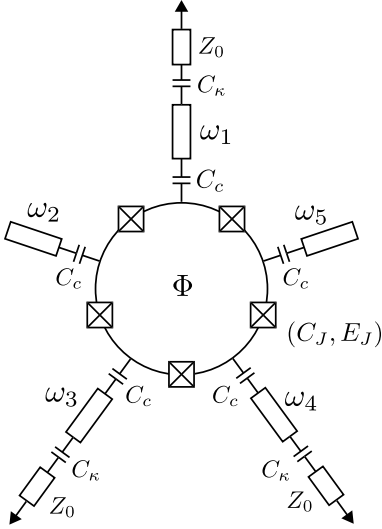


FIG. 23. Circuit diagram of a possible physical realization of the system depicted in Fig.6.  $Z_0$  is the characteristic impedance of the transmission lines.  $C_\kappa$  is the coupling capacitance between the resonators and the transmission lines.  $C_c$  is the coupling capacitance between the resonators and the Josephson ring.  $C_J$  and  $E_J$  are the junction capacitance and the Josephson energy, respectively.

The Hamiltonian of the system is represented by

$$H = H_{\text{res}} + H_{\text{Jring}} + H_{\text{int}}, \quad (\text{G1})$$

where  $H_{\text{res}}$ ,  $H_{\text{Jring}}$  and  $H_{\text{int}}$  respectively describe the resonators, the Josephson ring and their interaction.  $H_{\text{res}}$  is given by

$$H_{\text{res}} = \sum_{m=1}^5 \hbar \omega_m a_m^\dagger a_m, \quad (\text{G2})$$

and  $H_{\text{Jring}}$  is given by

$$H_{\text{Jring}} = \frac{1}{2} \vec{Q}^T \mathcal{C}^{-1} \vec{Q} + V(\vec{\phi}, \Phi), \quad (\text{G3})$$

with the charge vector  $\vec{Q}^T = (Q_1, Q_2, Q_3, Q_4, Q_5)$  and the flux vector  $\vec{\phi} = (\phi_1, \phi_2, \phi_3, \phi_4, \phi_5)$ , where  $Q_\mu$  and  $\phi_\mu$  are the charge and the flux on node  $\mu$  of the Josephson ring, respectively, and satisfy the commutation relation,  $[\phi_\mu, Q_\nu] = i\hbar \delta_{\mu,\nu}$ .  $\mathcal{C}$  is the capacitance matrix with matrix elements  $C_{\mu,\mu\pm 1} = -C_J$  and  $C_{\mu,\mu} = 2C_J + C_c$ , where  $C_J$  and  $C_c$  are the junction capacitance and the coupling capacitance between a resonator and the Josephson ring, respectively. The inductive energy is represented as

$$V(\vec{\phi}, \Phi) = -E_J \sum_{\mu=1}^5 \cos \left[ \frac{2\pi}{\Phi_0} (\phi_{\mu+1} - \phi_\mu - \Phi/5) \right], \quad (\text{G4})$$

with the Josephson energy  $E_J$ , where  $\mu$  is modulo 5, that

is,  $\mu = 6$  is identical to  $\mu = 1$ . The interaction Hamiltonian is given by

$$H_{\text{int}} = C_c \sum_m (\mathbf{e}_m^T \mathcal{C}^{-1} \vec{Q}) q_m \varphi_m, \quad (\text{G5})$$

where  $\mathbf{e}_m$  is the unit vector of which  $m$ -th element is unity and the others are zero, and  $q_m = \sqrt{\omega_m/2}(a_m + a_m^\dagger)$ , and  $\varphi_m$  is the amplitude of the mode function at the coupling capacitance  $C_c$ . In Eq. (G5),  $\mathbf{e}_m^T \mathcal{C}^{-1} \vec{Q}$  corresponds to the voltage of the superconductive island  $m$ , and  $q_m \varphi_m$  is the voltage at the end of resonator  $m$ .  $H_{\text{int}}$  can be represented also as  $H_{\text{int}} = C_c \vec{V}_{\text{ring}} \cdot \vec{V}_{\text{res}}$  with  $\vec{V}_{\text{ring}} = \mathcal{C}^{-1} \vec{Q}$  and  $\vec{V}_{\text{res}}^T = (q_1 \varphi_1, q_2 \varphi_2, \dots)$ . We rewrite Eq. (G5) as

$$H_{\text{int}} = 2eC_c \sum_{m,\mu} \xi_{m,\mu} V_{\text{rms}}^{(m)} n_\mu (a_m + a_m^\dagger), \quad (\text{G6})$$

where  $n_\mu = Q_\mu/(2e)$ , and  $\xi_{m,\mu} = [\mathcal{C}^{-1}]_{m,\mu}$ , and  $V_{\text{rms}}^{(m)} = \varphi_m \sqrt{\omega_m/2}$ .

Now we derive an effective photon lattice Hamiltonian in the dispersive regime, where the coupling between a resonator and the Josephson ring is sufficiently smaller than the energy difference between photonic and circuit excitations. We assume that the Josephson ring transfers microwaves via intermediate virtual excitations and remains in its ground state during the operation[16]. The effective Hamiltonian is obtained by the canonical transformation

$$\begin{aligned} H_{\text{ph}} &= P_0 e^{iS} H e^{-iS} P_0 \\ &= P_0 (H_{\text{res}} + H_{\text{Jring}}) P_0 + P_0 [iS, H_{\text{int}}] P_0 / 2 + O(H_{\text{int}}^3), \end{aligned} \quad (\text{G7})$$

where  $P_0$  is the projection operator onto the subspace in which the Josephson ring is in its ground state. Here,  $iS$  is defined by

$$iS = \sum_{\alpha,\alpha'} \frac{\langle \alpha' | H_{\text{int}} | \alpha \rangle}{E_{\alpha'} - E_\alpha} | \alpha' \rangle \langle \alpha | \quad (\text{G8})$$

with the eigenstates  $|\alpha\rangle, |\alpha'\rangle$  of  $H_{\text{res}} + H_{\text{Jring}}$  so that the first-order quantities in  $H_{\text{int}}$  are eliminated in  $H_{\text{ph}}$ . The second term in Eq. (G7) is of the second order in  $H_{\text{int}}$  and gives rise to the mutual couplings between resonators.

In Eq. (G6) we approximate  $n_\mu a_m$  and  $n_\mu a_m^\dagger$  by  $\sum_k n_{\mu,k} |N_0, k\rangle \langle N_0, 0| a_m$  and  $\sum_k n_{\mu,k}^* |N_0, 0\rangle \langle N_0, k| a_m^\dagger$ , respectively, where  $N_0$  is the relevant total charge of the Josephson ring which is conserved, and  $k (= 1, 2, \dots)$  runs over the excited states of the Josephson ring, and

$$n_{\mu,k} = \langle N_0, k | n_\mu | N_0, 0 \rangle. \quad (\text{G9})$$

Here,  $\sum_k n_{\mu,k} |N_0, k\rangle \langle N_0, 0| a_m$  annihilates a photon in resonator  $m$  and yields an excitation in the Josephson ring. This approximation is based on the assumption that the Josephson ring remains in its ground states, and we neglect the counter rotating terms. Then, the inter-

action Hamiltonian in Eq. (G5) is represented as

$$H_{\text{int}} = (2eC_c) \sum_{m,\mu,k} \xi_{m,\mu} V_{\text{rms}}^{(m)} n_{\mu,k} a_m |N_0, k\rangle \langle N_0, 0| + h.c.. \quad (\text{G10})$$

Using Eqs. (G7) and (G10), the effective photon lattice Hamiltonian is obtained as

$$H_{\text{ph}} = \sum_m \varepsilon_m a_m^\dagger a_m + \sum_{m,n(\neq m)} t_{m,n} a_m^\dagger a_n \quad (\text{G11})$$

with

$$\begin{aligned} \varepsilon_m &= \hbar\omega_m + (2eC_c)^2 \sum_{k>0} \left[ \frac{1}{\hbar\omega_m - E_k} |\Xi_{m,k}|^2 \right], \\ t_{mn} &= 2(eC_c)^2 \sum_{k>0} \left[ \left( \frac{1}{\hbar\omega_m - E_k} + \frac{1}{\hbar\omega_n - E_k} \right) \Xi_{m,k}^* \Xi_{n,k} \right], \end{aligned} \quad (\text{G12})$$

where

$$\Xi_{m,k} = V_{\text{rms}}^{(m)} \sum_{\mu} \xi_{m,\mu} n_{\mu k}. \quad (\text{G13})$$

Note that  $\varepsilon_m$  and  $t_{m,n}$  depend on  $\Phi$  through  $n_{\mu,k}$  in Eq. (G9). Therefore, the coupling among resonators can be tuned *in-situ* via  $\Phi$ . We consider the temporal modulation of  $\Phi$  around fixed value  $\Phi_0$ , that is,  $\Phi(t) = \Phi_0 + \Delta\Phi(t)$ . Then,  $t_{m,n}$  and  $\varepsilon_m$  are represented as

$$\begin{aligned} t_{m,n}(\Phi) &= t_{m,n}(\Phi_0) + \Delta t_{m,n}(\Delta\Phi), \\ \varepsilon_m(\Phi) &= \varepsilon_m(\Phi_0) + \Delta\varepsilon_m(\Delta\Phi). \end{aligned} \quad (\text{G14})$$

We consider a narrow range of  $\Delta\Phi$  in which  $\Delta t_{m,n}$  and  $\Delta\varepsilon_m$  are proportional to  $\Delta\Phi$ . Then, the time dependence of  $\Delta t_{m,n}$  and  $\Delta\varepsilon_m$  are represented as

$$\begin{aligned} \Delta t_{m,n}(t) &= \left. \frac{dt_{m,n}}{d\Phi} \right|_{\Phi_0} \Delta\Phi(t), \\ \Delta\varepsilon_m(t) &= \left. \frac{d\varepsilon_m}{d\Phi} \right|_{\Phi_0} \Delta\Phi(t). \end{aligned} \quad (\text{G15})$$

The coupling among resonators can be tuned via the time-dependence of  $\Delta\Phi(t)$ . We consider  $\Delta\Phi(t)$  represented by

$$\Delta\Phi(t) = \sum_l \Phi_l \cos(\Omega_l t + \theta_l), \quad (\text{G16})$$

where the index  $l$  runs over every pair of the resonators, and we set  $\Omega_l$  so that it matches to the difference of the resonance frequencies of resonator pair  $l$ . In the RWA the coupling strength between resonators  $m$  and  $n$  is represented as  $\frac{1}{2} \frac{dt_{m,n}}{d\Phi} \Phi_{l=(m,n)} e^{-i\theta_{l=(m,n)}}$ . We assume that the influence of the second term of  $\varepsilon_m(t)$  is negligible in the RWA because it is rapidly oscillating.

Several comments are in order. (i) Although the evaluation of  $\varepsilon_m$  and  $t_{m,n}$  exceeds the scope of this paper,

it was reported that  $|t_{m,n}|/(2\pi)$  can exceed 20 MHz for  $N = 3$  depending on  $\Phi$  [16]. The frequency corresponding to the excitation energy from the ground state of the Josephson ring can be higher than 10 GHz. Thus, excitation of the Josephson ring induced by oscillating  $\Phi$  with frequency of orders of 100 MHz is negligible. (ii)  $\Omega_l$  is chosen such that the oscillating  $\Phi$  couples resonators. Each pair of the resonators should have different frequency difference for selective coupling. This limits the number of resonators. (iii) The electric potentials of the superconducting islands can be tuned via gate voltages to optimize the resonator coupling strength, although we consider the case that the gate voltages are zero for the simplicity.

A comment on the realization of the GR hopping is in order. The way discussed above utilizes a single coupler and the oscillating field with  $N(N-1)/2$  modulation frequencies. However, using many modulation frequencies will be challenging and inconvenient. In Ref. 16, a way to realize complex hopping between resonators was introduced using a Josephson ring coupler with static fields. The static magnetic field penetrating the Josephson ring and the electric potential of the superconducting islands are used to tune the amplitude and the phase of the complex hopping. Such coupler with static fields could possibly be used for coupling of each resonator pair alternatively, although it may make fabrication more challenging. Design of the circulator which is more experimentally feasible will be studied elsewhere.

## Appendix H: Noise spectra

The effect of noise is studied by taking into account internal dissipation of resonators. The internal dissipation is modeled by a fictional transmission line attached to each resonator. The Heisenberg equation of motion of  $a_m$  is represented as

$$\begin{aligned} \frac{d}{dt} a_m &= \left( -i\omega_m - \frac{(\kappa_m + \kappa_m^{(\text{int})})}{2} \right) a_m - i \sum_{n(\neq m)} g_{m,n}(t) a_n \\ &\quad - i\sqrt{v\kappa_m} \tilde{b}_{m,vt}^{(\text{in})} - i\sqrt{v\kappa_m^{(\text{int})}} \tilde{c}_{m,vt}^{(\text{in})}, \end{aligned} \quad (\text{H1})$$

where  $\tilde{b}_{m,vt}^{(\text{in})}$  is the real-space representation of the transmission line fields defined by Eq. (B3), and  $\tilde{c}_{m,vt}^{(\text{in})}$  is defined analogously for the mode corresponding to internal dissipation of resonator  $m$ .  $\kappa_m^{(\text{int})}$  is the internal decay rate.

Moving to the frame rotating at resonator frequencies, the Heisenberg equation of motion is written as

$$\begin{aligned} \frac{d}{dt} a_m &= -\frac{(\kappa_m + \kappa_m^{(\text{int})})}{2} a_m - i \sum_{n(\neq m)} \bar{g}_{m,n} e^{-i\theta_{m,n}} a_n \\ &\quad - i\sqrt{v\kappa_m} \tilde{b}_{m,vt}^{(\text{in})} - i\sqrt{v\kappa_m^{(\text{int})}} \tilde{c}_{m,vt}^{(\text{in})}. \end{aligned} \quad (\text{H2})$$

Fourier transformation of the above equation leads to

$$\sum_n \mathcal{G}_{mn} a_n(\omega) = -i\sqrt{v\kappa_m} \tilde{b}_m^{(\text{in})}(\omega) - i\sqrt{v\kappa_m^{(\text{int})}} \tilde{c}_m^{(\text{in})}(\omega), \quad (\text{H3})$$

where

$$\mathcal{G}_{m,n} = \begin{cases} (\kappa_m + \kappa_m^{(\text{int})})/2 - i\omega & (n = m) \\ i\tilde{g}_{m,n} e^{-i\theta_{m,n}} & (n \neq m). \end{cases} \quad (\text{H4})$$

Here,  $\omega$  is the detuning of the input field and identical to  $\Delta\omega$  in Eq. (8).

Using Eq. (H3), we obtain

$$\vec{a}(\omega) = -i\sqrt{v}[\mathcal{G}^{-1}][\vec{b}^{(\text{in})}(\omega) + \vec{c}^{(\text{in})}(\omega)], \quad (\text{H5})$$

where  $\vec{a}(\omega) = (a_1(\omega), \dots, a_N(\omega))^T$ ,  $\vec{b}^{(\text{in})}(\omega) = (\sqrt{\kappa_1} \tilde{b}_1^{(\text{in})}(\omega), \dots, \sqrt{\kappa_N} \tilde{b}_N^{(\text{in})}(\omega))^T$  and  $\vec{c}^{(\text{in})}(\omega) = (\sqrt{\kappa_1} \tilde{c}_1^{(\text{in})}(\omega), \dots, \sqrt{\kappa_N} \tilde{c}_N^{(\text{in})}(\omega))^T$ , respectively. Equivalently,  $a_m(\omega)$  is represented as

$$a_m(\omega) = -i\sqrt{v} \sum_n [\mathcal{G}^{-1}]_{m,n} \left[ \sqrt{\kappa_n} \tilde{b}_n^{(\text{in})}(\omega) + \sqrt{\kappa_n^{(\text{int})}} \tilde{c}_n^{(\text{in})}(\omega) \right]. \quad (\text{H6})$$

Substitution of Eq. (H6) into the input-output relation:

$$\tilde{b}_m^{(\text{out})}(\omega) = \tilde{b}_m^{(\text{in})}(\omega) - i\sqrt{\frac{\kappa_m}{v}} a_m(\omega) \quad (\text{H7})$$

leads to

$$\tilde{b}_m^{(\text{out})}(\omega) = \sum_n \left( S_{nm}^{(b)} \tilde{b}_n^{(\text{in})}(\omega) + S_{nm}^{(c)} \tilde{c}_n^{(\text{in})}(\omega) \right), \quad (\text{H8})$$

where

$$\begin{aligned} S_{nm}^{(b)} &= \delta_{m,n} - \sqrt{\kappa_m \kappa_n} [\mathcal{G}^{-1}]_{m,n}, \\ S_{nm}^{(c)} &= -\sqrt{\kappa_m \kappa_n^{(\text{int})}} [\mathcal{G}^{-1}]_{m,n}. \end{aligned} \quad (\text{H9})$$

$S_{n,m}^{(b)}$  is the same as  $S_{p,m}$  in Eq. (7), when  $n = p$  and there is no internal dissipation,  $\kappa_n^{(\text{int})} = 0$ .

The output noise spectral density of resonator  $m$  is

defined by [30, 45]

$$P_m^{(\text{out})}(\omega) = \frac{1}{2} \int_{-\infty}^{\infty} dt \left[ e^{i\omega t} \langle \tilde{b}_m^{(\text{out})}(t) \tilde{b}_m^{(\text{out})\dagger}(0) + \tilde{b}_m^{(\text{out})\dagger}(0) \tilde{b}_m^{(\text{out})}(t) \rangle \right]. \quad (\text{H10})$$

Using

$$\tilde{b}_m^{(\text{out})}(\omega) = \frac{1}{\sqrt{2\pi}} \int_{-\infty}^{\infty} dt e^{i\omega t} \tilde{b}_m^{(\text{out})}(t), \quad (\text{H11})$$

Eq. (H10) can be written as

$$P_m^{(\text{out})}(\omega) = \frac{1}{2} \int_{-\infty}^{\infty} d\omega' \langle \tilde{b}_m^{(\text{out})}(\omega) [\tilde{b}_m^{(\text{out})}(\omega')]^\dagger + [\tilde{b}_m^{(\text{out})}(\omega')]^\dagger \tilde{b}_m^{(\text{out})}(\omega) \rangle. \quad (\text{H12})$$

We assume that the bath is probed only in a narrow range of frequencies centered at  $\omega_m$  and use the relation of the input bosonic operators [30, 45]:

$$\begin{aligned} \langle \tilde{b}_m^{(\text{in})}(t) (\tilde{b}_m^{(\text{in})}(t'))^\dagger \rangle &= (\bar{n}_m^{(b)} + 1) \delta(t - t'), \\ \langle \tilde{c}_m^{(\text{in})}(t) (\tilde{c}_m^{(\text{in})}(t'))^\dagger \rangle &= (\bar{n}_m^{(c)} + 1) \delta(t - t'), \end{aligned} \quad (\text{H13})$$

where the thermal equilibrium occupation number,  $\bar{n}_m^{(b/c)}$ , is given by

$$\bar{n}_m^{(b/c)} = \frac{1}{\exp[\hbar\omega_m / (k_B T_m^{(b/c)})] - 1} \quad (\text{H14})$$

with the temperature of the actual or fictional transmission line  $T_m^{(b/c)}$  attached to resonator  $m$ . Using Eq. (H13) and

$$\begin{aligned} \tilde{b}_m^{(\text{in})}(\omega) &= \frac{1}{\sqrt{2\pi}} \int_{-\infty}^{\infty} dt e^{i\omega t} \tilde{b}_m^{(\text{in})}(t), \\ \tilde{c}_m^{(\text{in})}(\omega) &= \frac{1}{\sqrt{2\pi}} \int_{-\infty}^{\infty} dt e^{i\omega t} \tilde{c}_m^{(\text{in})}(t), \end{aligned} \quad (\text{H15})$$

we obtain

$$\begin{aligned} \langle \tilde{b}_m^{(\text{in})}(\omega) (\tilde{b}_m^{(\text{in})}(\omega'))^\dagger \rangle &= (\bar{n}_m^{(b)} + 1) \delta(\omega - \omega'), \\ \langle \tilde{c}_m^{(\text{in})}(\omega) (\tilde{c}_m^{(\text{in})}(\omega'))^\dagger \rangle &= (\bar{n}_m^{(c)} + 1) \delta(\omega - \omega'). \end{aligned} \quad (\text{H16})$$

Using Eqs. (H8), (H12) and (H16),  $P_m^{(\text{out})}(\omega)$  in Eq. (H10) is represented as

$$P_m^{(\text{out})}(\omega) = \sum_{n,\alpha} \left\{ |S_{nm}^{(\alpha)}(\omega)|^2 \left( \bar{n}_n^{(\alpha)} + \frac{1}{2} \right) \right\}, \quad (\text{H17})$$

where  $\alpha$  runs over  $b$  and  $c$ .

- 
- [1] A. Blais, R.-S. Huang, A. Wallraff, S. M. Girvin and R. J. Schoelkopf, Phys. Rev. A **69**, 062320 (2004).  
 [2] A. Wallraff, D. I. Schuster, A. Blais, L. Frunzio, R.-S. Huang, J. Majer, S. Kumar, S. M. Girvin, and R. J. Schoelkopf, Nature **431**, 162 (2004).

- [3] O. Astafiev, K. Inomata, A. O. Niskanen, T. Yamamoto, Y. A. Pashkin, Y. Nakamura and J. S. Tsai, Nature **449**, 588–590 (2007).  
 [4] M. Hofheinz, H. Wang, M. Ansmann, R. C. Bialczak, E. Lucero, M. Neeley, A. D. O’Connell, D. Sank, J. Wen-

- ner, J. M. Martinis and A. N. Cleland, *Nature* **459**, 546 (2009).
- [5] K. Inomata, Z. R. Lin, K. Koshino, W. D. Oliver, J. S. Tsai, T. Yamamoto and Y. Nakamura, *Nat. Commun.* **7**, 7, 12303 (2016).
- [6] K. Y. Tan, M. Partanen, R. E. Lake, J. Govenius, S. Masuda and M. Möttönen, *Nat. Commun.* **8**, 15189 (2017).
- [7] Y. Nakamura, Yu. A. Pashkin and J. S. Tsai, *Nature* **398**, 786–788 (1999).
- [8] O. Astafiev, A. M. Zagoskin, A. A. Abdumalikov, Jr., Y. A. Pashkin, T. Yamamoto, K. Inomata, Y. Nakamura, and J. S. Tsai, *Science* **327**, 840 (2010).
- [9] E. L. Wolf, *Quantum Nanoelectronics: An Introduction to Electronic Nanotechnology and Quantum Computing*; (Wiley-VCH, Weinheim, 2009).
- [10] J. Majer, J. M. Chow, J. M. Gambetta, J. Koch, B. R. Johnson, J. A. Schreier, L. Frunzio, D. I. Schuster, A. A. Houck, A. Wallraff, A. Blais, M. H. Devoret, S. M. Girvin, and R. J. Schoelkopf, *Nature* **449**, 443 (2007).
- [11] M. A. Sillanpää, J. I. Park and R. W. Simmonds, *Nature* **449**, 438 (2007).
- [12] M. H. Devoret and R. J. Schoelkopf, *Science* **339**, 1169 (2013).
- [13] J. Kelly et al., *Nature* **519**, 66 (2015).
- [14] N. Ofek, et al., *Nature* **536**, 441 (2016).
- [15] K. Koshino, K. Inomata, Z. R. Lin, Y. Tokunaga, T. Yamamoto and Y. Nakamura, *Phys. Rev. Applied* **7**, 064006 (2017).
- [16] J. Koch, A. A. Houck, K. L. Hur, and S. M. Girvin, *Phys. Rev. A* **82** 043811 (2010).
- [17] A. Kamal, J. Clarke, and M. Devoret, *Nat. Phys.* **7**, 311 (2011).
- [18] A. Nunnenkamp, J. Koch, and S. M. Girvin, *New J. Phys.* **13**, 095008 (2011).
- [19] M. Hafezi and P. Rabi, *Opt. Express* **20**, 7672–7684 (2012).
- [20] J. Kerckhoff, K. Lalumière, B. J. Chapman, A. Blais and K. W. Lehnert, *Phys. Rev. Applied.* **4**, 034002 (2015).
- [21] A. Metelmann and A. A. Clerk, *Phys. Rev. X* **5**, 021025 (2015).
- [22] L. Ranzani and J. Aumentado, *New J. Phys.* **17**, 023024 (2015).
- [23] S. Walter and F. Marquardt, *New J. Phys.* **18**, 113029 (2016).
- [24] H. Lira, Z. Yu, S. Fan and M. Lipson, *Phys. rev. Lett.* **109**, 033901 (2012).
- [25] K. M. Sliwa, M. Hatridge, A. Narla, S. Shankar, L. Frunzio, R. J. Schoelkopf, and M. H. Devoret, *Phys. Rev. X* **5**, 041020 (2015).
- [26] M. Scheucher, A. Hilico, E. Will, J. Volz and A. Rauschenbeutel, *Science* **354** 1577 (2016).
- [27] P. Roushan et al., *Nat. Phys.* **13**, 146 (2017).
- [28] B. J. Chapman, E. I. Rosenthal, J. Kerckhoff, B. A. Moores, L. R. Vale, J. A. B. Mates, G. C. Hilton, K. Lalumière, A. Blais and K. W. Lehnert, *Phys. Rev. X* **7**, 041043 (2017).
- [29] G. A. Peterson, F. Lecocq, K. Cicak, R. W. Simmonds, J. Aumentado and J. D. Teufel, *Phys. Rev. X* **7**, 031001 (2017).
- [30] N. R. Bernier, L. D. Tóth, A. Koottandavida, M. A. Ioannou, D. Malz, A. Nunnenkamp, A. K. Feofanov and T. J. Kippenberg, *Nat. Commun.* **8**, 604 (2017).
- [31] S. Barzanjeh, M. Wulf, M. Peruzzo, M. Kalaei, P. B. Dieterle, O. Painter and J. M. Fink, *Nat. Communications* **8**, 953 (2017).
- [32] A. Metelmann and H. E. Türeci, arXiv:1703.04052v1 (2017).
- [33] K. Fang, Z. Yu, and S. Fan, *Nat. Photon.* **6**, 782 (2012).
- [34] F. Gebhard and A. E. Ruckenstein, *Phys. Rev. Lett.* **68**, 244 (1992).
- [35] Y. Kuramoto and Y. Kato, *One-Dimensional Quantum Systems* (Cambridge, London, 2009).
- [36] S. Masuda and Y. Kuramoto, *Phys. Rev. B* **85**, 195327 (2012).
- [37] M. Hafezi, P. Adhikari and J. M. Taylor, *Phys. Rev. B* **90**, 060503 (2014).
- [38] E. Kapit, *Phys. Rev. A* **92**, 012302 (2015).
- [39] D. Jaksch and P. Zoller, *New J. Phys.* **5**, 56 (2003).
- [40] M. Aidelsburger, M. Atala, M. Lohse, J. T. Barreiro, B. Paredes and I. Bloch, *Phys. Rev. Lett.* **111**, 185301 (2013).
- [41] H. Miyake, G. A. Siviloglou, C. J. Kennedy, W. C. Burton, and W. Ketterle, *Phys. Rev. Lett.* **111**, 185302 (2013).
- [42] A. Kamal and A. Metelmann, *Phys. Rev. Applied* **7**, 034031 (2017).
- [43] K. Koshino and Y. Nakamura, *New J. Phys.* **14**, 043005 (2012).
- [44] K. Koshino, K. Inomata, T. Yamamoto and Y. Nakamura, *New J. Phys.* **15**, 115010 (2013).
- [45] A.A. Clerk, M. H. Devoret, S. M. Girvin, F. Marquardt and R. J. Schoelkopf, *Rev. Mod. Phys.* **82**, 1155 (2010).